# Synergic Thermo- and pH-Sensitive Hybrid Microgels Loaded with Fluorescent Dyes and Ultrasmall Gold Nanoparticles for Photoacoustic Imaging and Photothermal Therapy

Yu Xiao, Kartikey Pandey, Alba Nicolás-Boluda, Delphine Onidas, Philippe Nizard, Florent Carn, Théotim Lucas, Jérôme Gateau, Alberto Martin-Molina, Manuel Quesada-Pérez, et al.

## To cite this version:

Yu Xiao, Kartikey Pandey, Alba Nicolás-Boluda, Delphine Onidas, Philippe Nizard, et al.. Synergic Thermo- and pH-Sensitive Hybrid Microgels Loaded with Fluorescent Dyes and Ultrasmall Gold Nanoparticles for Photoacoustic Imaging and Photothermal Therapy. ACS Applied Materials & Interfaces, 2022, 14 (49), pp.54439-54457. 10.1021/acsami.2c12796 . hal-03855214

**HAL Id: hal-03855214**
**https://hal.science/hal-03855214v1**

Submitted on 16 Nov 2022

# Synergic Thermo- and pH-Sensitive Hybrid Microgels Loaded with Fluorescent Dyes and Ultrasmall Gold Nanoparticles for Photoacoustic Imaging and Photothermal Therapy

Yu Xiao[a], Kartikey Pandey[a], Alba Nicolás-Boluda[b], Delphine Onidas[a], Philippe Nizard[a], Florent Carn[b], Théotim Lucas[b,c], Jérôme Gateau[c], Alberto Martin-Molina[e,f], Manuel Quesada-Pérez[g], Maria del Mar Ramos-Tejada[g], Florence Gazeau*[b], Yun Luo*[a], Claire Mangeney *[a]

a. Université Paris Cité, CNRS Laboratoire de Chimie et de Biochimie Pharmacologiques et Toxicologiques, F-75006 Paris, France

b. Université Paris Cité, CNRS Matière et Systèmes Complexes MSC, F-75006 Paris, France.

c. Sorbonne Université, CNRS, INSERM, Laboratoire d'Imagerie Biomédicale, LIB, F-75006, Paris, France

e. Departamento de Física Aplicada, Universidad de Granada, Campus de Fuentenueva s/n, 18071 Granada, Spain

f. Instituto Carlos I de Física Teórica y Computacional, Universidad de Granada, Campus de Fuentenueva s/n, 18071 Granada, Spain

g. Departamento de Física, Escuela Politécnica Superior de Linares, Universidad de Jaén, 23700, Linares, Jaén, Spain

## ABSTRACT

Smart microgels (μGels) made of polymeric particles doped with inorganic nanoparticles have emerged recently as promising multifunctional materials for nanomedicine applications. However, the synthesis of these hybrid materials is still a challenging task with the necessity to control several features, such as particle sizes and doping levels in order to tailor their final properties in relation to the targeted application. We report herein an innovative modular strategy to achieve the rational design of well-defined and densely filled hybrid particles. It is based on the assembly of the different building blocks, *i.e.* µGels, dyes and small gold nanoparticles (< 4 nm) and the tuning of nanoparticle loading within the polymer matrix through successive incubation steps. The characterization of the final hybrid networks using UV-vis absorption, fluorescence, transmission electron microscopy, dynamic light scattering and small angle X-ray scattering revealed that they uniquely combine the properties of hydrogel particles, including high loading capacity and stimuli-responsive behavior, the photoluminescent properties of dyes (rhodamine 6G, methylene blue and cyanine 7.5) and the features of gold nanoparticles assembly. Interestingly, in response to pH and temperature stimuli, the smart hybrid µGels can shrink, leading to the aggregation of the gold nanoparticles trapped inside the polymer matrix. This stimuli-responsive behavior results in plasmon band broadening and red shift towards the near infrared region (NIR), opening promising prospects in biomedical science. Particularly, the potential of these smart hybrid nanoplatforms for photo-activated hyperthermia, photoacoustic imaging, cellular internalization, intracellular imaging and photothermal therapy was assessed, demonstrating well controlled multimodal opportunities for theranostics.

**KEYWORDS:** Gold nanoparticles, pH and temperature sensitive microgels, fluorescent dyes, photoacoustic imaging, photothermal therapy, NIR-enhanced.

## 1. INTRODUCTION

The development of hybrid microgels (µGels) based on the integration of inorganic nanoparticles into polymeric particles has stimulated worldwide efforts in recent years due to their promising biomedical applications as smart therapeutic systems, bioimaging agents [1, 2] or antibacterial materials[3]. These materials combine the unique properties of hydrogel particles, including softness, deformability, drug-loading capacity and stimuli-responsive behavior and the outstanding features of nanoparticles (NPs) with optical, magnetic, electronic or catalytic activities. Two main strategies have been explored to synthesize hybrid μGels [4]: (i) the growth of NPs *in situ* in the presence of polymeric μGels; (ii) the synthesis of inorganic NPs *ex situ* followed by their incorporation inside the polymer matrix. Although the first approach has stimulated a wide interest[5, 6] owing to its simplicity, it results in a poor control over the size and morphology of the inorganic NPs. In contrast, the second approach offers a unique opportunity to achieve a preliminary control of the colloidal characteristics (size, polydispersity, surface functionalities) of each separate building blocks (μGels and inorganic NPs)[7, 8]. However, it has received very little attention up to now due to the difficulties in obtaining large amounts of NPs trapped inside the microgel matrix while preventing their aggregation and leaking. Therefore, the development of a versatile strategy to achieve the self-assembly of separate preformed colloidal particles still remains challenging.

We propose here an innovative modular strategy to finely tune the loading density of inorganic NPs within the polymer matrix via successive incubation steps, from one to five times, leading to densely filled μGels. As a proof of concept, a polymer matrix based on copolymers of oligo(ethylene glycol) methyl ether methacrylate and methacrylic acid was chosen to provide a polyanionic building block with swelling/deswelling response, pH- and thermo-sensitive behavior, desirable colloidal stability and biodegradability[7-9]. Besides, oligo(ethylene glycol) methacrylate based copolymers are interesting with respect to the criterion of biocompatibility[10, 11] and oligo(methacrylic acid) residues have been approved by the FDA (Food and Drug Administration) for drug delivery capsules. To impart fluorescence properties to the μGels, three different dyes were loaded within the hydrogel matrix: rhodamine 6G (R6G), methylene blue (MB) and cyanine 7.5 (Cy), resulting in microparticles with optical emission extending from the visible to the NIR range. Gold NPs (Au NPs) coated with citrates were selected as the inorganic building blocks due to their outstanding optical properties[12], based on the collective oscillations of free electrons at the particle surface, resulting in so-called localized surface plasmon resonances (LSPR). Upon light excitation of LSPR, a strong electromagnetic field enhancement is produced at the NP surface, leading to a wide range of applications in the fields of biology and chemistry, including surface enhanced Raman spectroscopy (SERS), bioimaging and sensing[13]. In addition, Au NPs are able to convert the absorbed light into heat through non-radiative energy dissipation, making them valuable light-to-heat plasmonic converters for biomedical hyperthermia, cancer treatments or antibacterial assays[14]. Regarding nanotoxicity, sub-6 nm gold nanospheres are interesting candidates as they have been shown to undergo biodegradation and they can be excreted via the kidneys, which is a key parameter for clinical translation[15-17]. However, the plasmon resonance wavelength of gold nanospheres is located in the visible region, which limits their interest for *in vivo* applications. Although the optical resonances of anisotropic gold NPs such as nanostars[18] or nanorods[19] lie favorably in the NIR, their poor biodegradation and persistent accumulation in the body have raised some concerns about their potential long term toxicity. Therefore, the combination of NIR optical absorption and bioelimination properties is still an important issue. It was addressed recently by designing dense assemblies of small spherical Au NPs with short double-strand DNA, resulting in plasmon coupling between individual NPs and efficient plasmon absorption at NIR wavelengths[20]. The approach described herein offers a versatile alternative to obtain dense assemblies of small Au NPs within fluorescent multifunctional microparticles, which could be compared to the assembly of lego® bricks (see Figure 1). The first step consists in the loading of dyes within μGels, while the second step is the uptake of Au NPs, through successive incubation steps, promoting a high loading density. The samples were experimentally characterized by UV-vis absorption, fluorescence spectroscopy, transmission electron microscopy (TEM), dynamic light scattering (DLS) and small angle X-ray scattering (SAXS). Moreover, the mechanism driving the assembly of the μGels, dyes and Au NPs was studied theoretically using coarse-grained simulations[21, 22] to understand the fundamental role played by diffusion and short-ranged attractive Van der Waals interactions in the absorption of NPs by the μGels. The potential of the final hybrid networks for biomedical science was then assessed through photothermal experiments, intracellular fluorescence microscopy, cell viability assays and photoacoustic spectroscopy. The fluorescent properties of the hybrid µGels could be used to track their uptake by cells while they also exhibit high molar absorption coefficients at λ = 800 nm, a key feature for photoacoustic (PA) imaging and photothermal therapy (PTT). Interestingly, pH and temperature stimuli could induce the shrinkage of the smart hybrid µGels resulting in Au NPs aggregation, plasmon coupling and improved absorption in the NIR region. Therefore, the final hybrid networks not only combine the remarkable features of each component but also display synergetic properties that open promising prospects for a broad range of bio-medical applications.

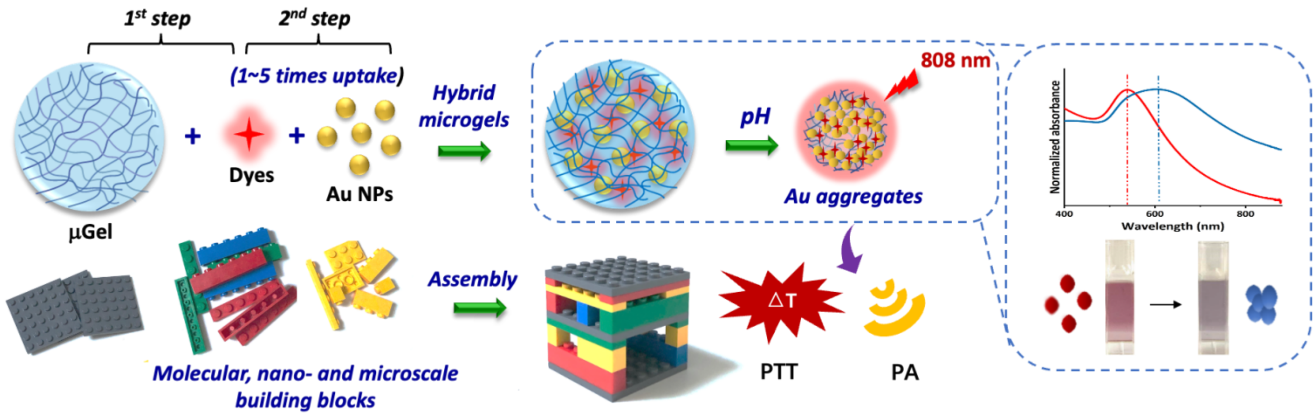

**Figure 1.** Representative scheme of the combination and assembly of µGels, fluorescent dyes and inorganic NPs (Au NPs). This approach provides a versatile toolbox to design a large variety of hybrid µGels, which can be compared to the assembly of Lego® bricks, as illustrated at the bottom of the figure.

## 2. RESULTS AND DISCUSSION

### 2.1 Synthesis of smart hybrid microgels

The µGels were synthesized from oligo(ethylene glycol) methyl ether methacrylate monomers and methacrylic acid by surfactant-free precipitation polymerization in water solvent, as described by N. Griffete *et al.* [8] (see details in SI part 1.3). Highly monodisperse spherical µGels were obtained using this method (see TEM images in Fig. S1a, b), with a mean hydrodynamic diameter ($D_h$) of 592 nm (polydispersity index = 0.1), measured from DLS at 20°C and pH 7.5. They were negatively charged at physiological pH (ζ potential = - 32 mV), due to the presence of carboxylic acid groups, which are deprotonated [$pK_a$ ~

4.8]. The polyanionic μGels could trap the fluorescent dyes (R6G, MB, Cy) after simple mixing of the microgel dispersion with dye solutions, in the same way as reported elsewhere for other types of hydrogel particles[23, 24]. As shown in Fig. 2, the resulting fluorophore-loaded μGels displayed the optical properties of each selected dye with absorption bands in the visible and NIR region ($\lambda_{Abs[R6G]}$ = 537 nm, $\lambda_{Abs[MB]}$ = 665 nm and $\lambda_{Abs[Cy]}$ = 795 nm) and distinct fluorescence emission peaks at $\lambda_{F[R6G]}$ = 560 nm, $\lambda_{F[MB]}$ = 686 nm and $\lambda_{F[Cy]}$ = 815 nm. It is noteworthy that the extinction spectra of Gel@dyes reveal some degree of dye aggregation within the μGels, particularly for MB at high dye concentration[25]. The excess of dyes (free dyes in solution) was removed by 1 cycle of centrifugation/redispersion and the supernatant was analyzed by UV−vis spectrophotometry to deduce the amount of dyes encapsulated within the μGels ($Dye_{uptake}$, eq. 1) and the loading efficiency (eq. 2).

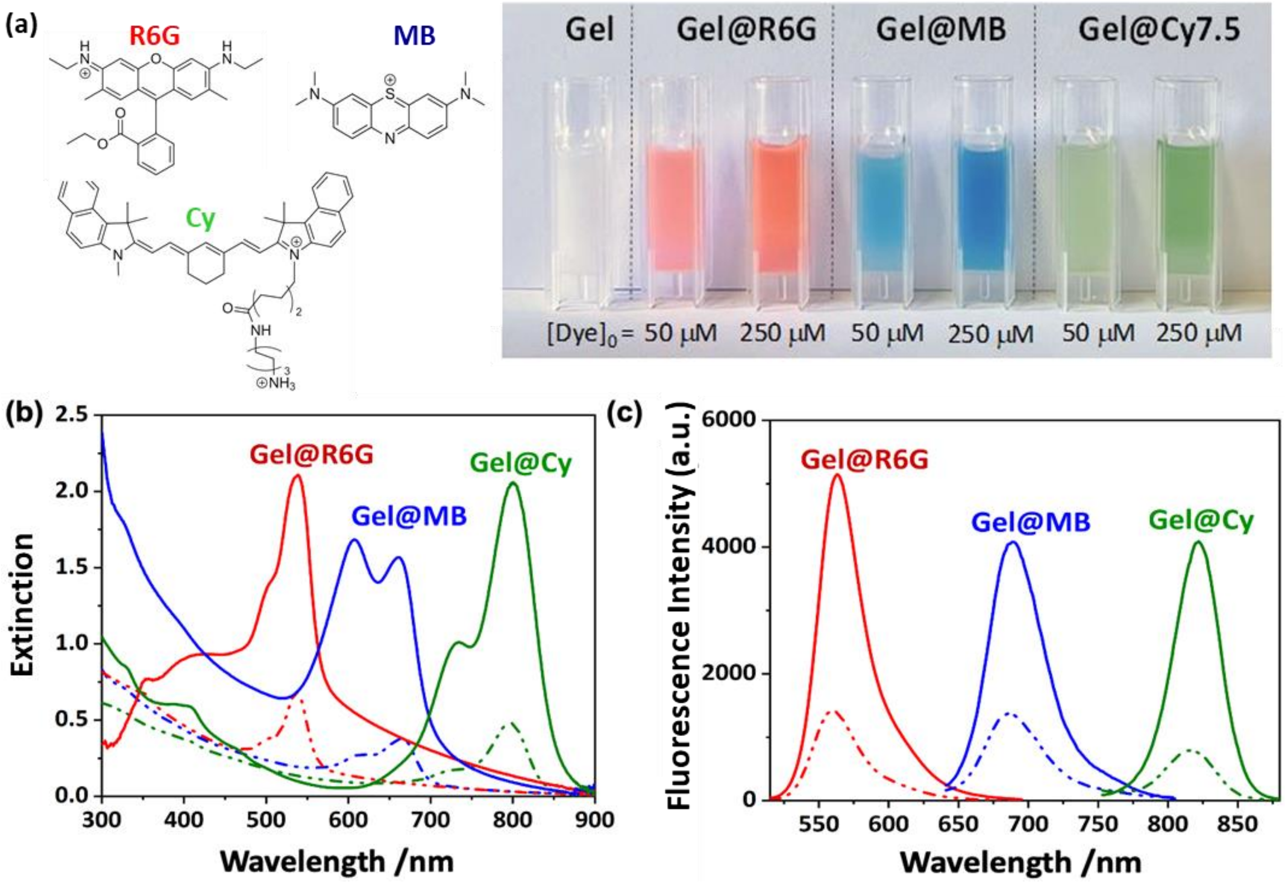

**Figure 2.** (a) Chemical structure of the dyes and digital pictures of Gel@dye dispersions, prepared with initial dye concentrations $[Dye]_0$ = 50 μM or $[Dye]_0$ = 250 μM. (b) UV-vis spectra of the various Gel@dye samples at [Gel@dye] = 0.04 nM, for an optical path length of 1 cm and (c) corresponding fluorescence spectra ($\lambda_{ex[R6G]}$ = 490

nm, $\lambda_{ex[MB]}$ = 610 nm, $\lambda_{ex[Cy]}$ = 716 nm). The dotted lines in (b) and (c) correspond to an initial dye concentration $[Dye]_0$ of 50 μM, while the continuous lines correspond to an initial dye concentration $[Dye]_0$ of 250 μM.

The dye loading efficiency reached *ca.* 94-100 % and the total amount of dyes loaded within the μGels could be tailored from 2.8 ± 0.1 to 14.2 ± 0.2 μmol of dyes per gram of μGels, depending on the type of dyes and their initial concentration in the reaction mixture, as shown in Table 1.

$$Dye_{uptake} = \frac{\text{initial amount of dyes (mol)} - \text{excess amount of dyes (mol)}}{mass\ of microgels\ (g)} \quad \text{(eq. 1)}$$

$$\text{Loading efficiency}(\%) = \frac{\text{initial amount of dyes (mol)} - \text{excess amount of dyes (mol)}}{initial\ amount\ of\ dyes\ (mol)} \times 100 \quad \text{(eq. 2)}$$

The zeta potential values of Gel@R6G, Gel@MB and Gel@Cy were equal to -32 mV, -30 mV and -28 mV, respectively, revealing a very slight increase compared to bare μGels, probably due to the small amount of cationic dyes and to their entrapment inside the negatively charged polymer network. The dye-loaded μGels were then mixed with citrate-coated Au NPs (diameter 3.8 ± 0.9 nm, Fig. S1c,d), yielding hybrid μGels doped with both fluorescent molecules and plasmonic NPs (TEM images Fig. 3).

**Table 1.** Dye and Au NPs uptake ($Dye_{uptake}$ and $AuNPs_{uptake}$) and loading efficiency into μGels.

| Dye | **$Dye_{uptake}$** (μmol of dyes per g of μGels) in Gel@dye | **$AuNPs_{uptake}$**(mg of Au NPs per g of μGels) in Gel@dye@$Au_{(X)}$ | | |
|---|---|---|---|---|
| | | **x=1** | **x=3** | **x=5** |
| | ***Loading efficiency in bracket*** | | | |
| **$[R6G]_0$ = 50 μM**<br>**$[R6G]_0$ = 250 μM** | 2.8 ± 0.1 (99%)<br>14.2 ± 0.2 (96%) | ~ 50 (100%)$^b$ | ~ 150 (100%) $^b$ | ~ 250 (100%) $^b$ |
| **$[MB]_0$ = 50 μM**<br>**$[MB]_0$ = 250 μM** | 2.8 ± 0.1 (99%)<br>13.9 ± 0.3 (96%) | | | |
| **$[Cy]_0$ = 50 μM**<br>**$[Cy]_0$ = 250 μM** | 2.9$^a$ (100%)<br>13.6 ± 0.4 (94%) | | | |

$^a$In the case of Gel@Cy, no absorption peak of cyanine could be detected in the supernatant after centrifugation, leading to an estimated dye loading efficiency of 100%. $^b$The absorption peak of Au NPs in the supernatant after centrifugation was so weak for both $[Dye]_0$ = 50 and 250 μM, that the Au NPs loading efficiency was estimated to be approximately 100%.

Interestingly, the total amount of Au NPs uptaken by the μGels could be finely tuned by performing several incubation experiments (number of incubation steps noted as x in Table 1 and Fig. 3), according to the following procedure: (i) mixing of Gel@dye with Au NPs solution ([Au NPs] = 0.27 μmol.L$^{-1}$); (ii) washing of the resulting μGels *via* one cycle of centrifugation/redispersion; (iii) mixing of the Gel@dye@Au samples obtained in the previous step with fresh solutions of Au NPs. This three-steps process was repeated up to five times, leading to μGels densely filled with Au NPs.

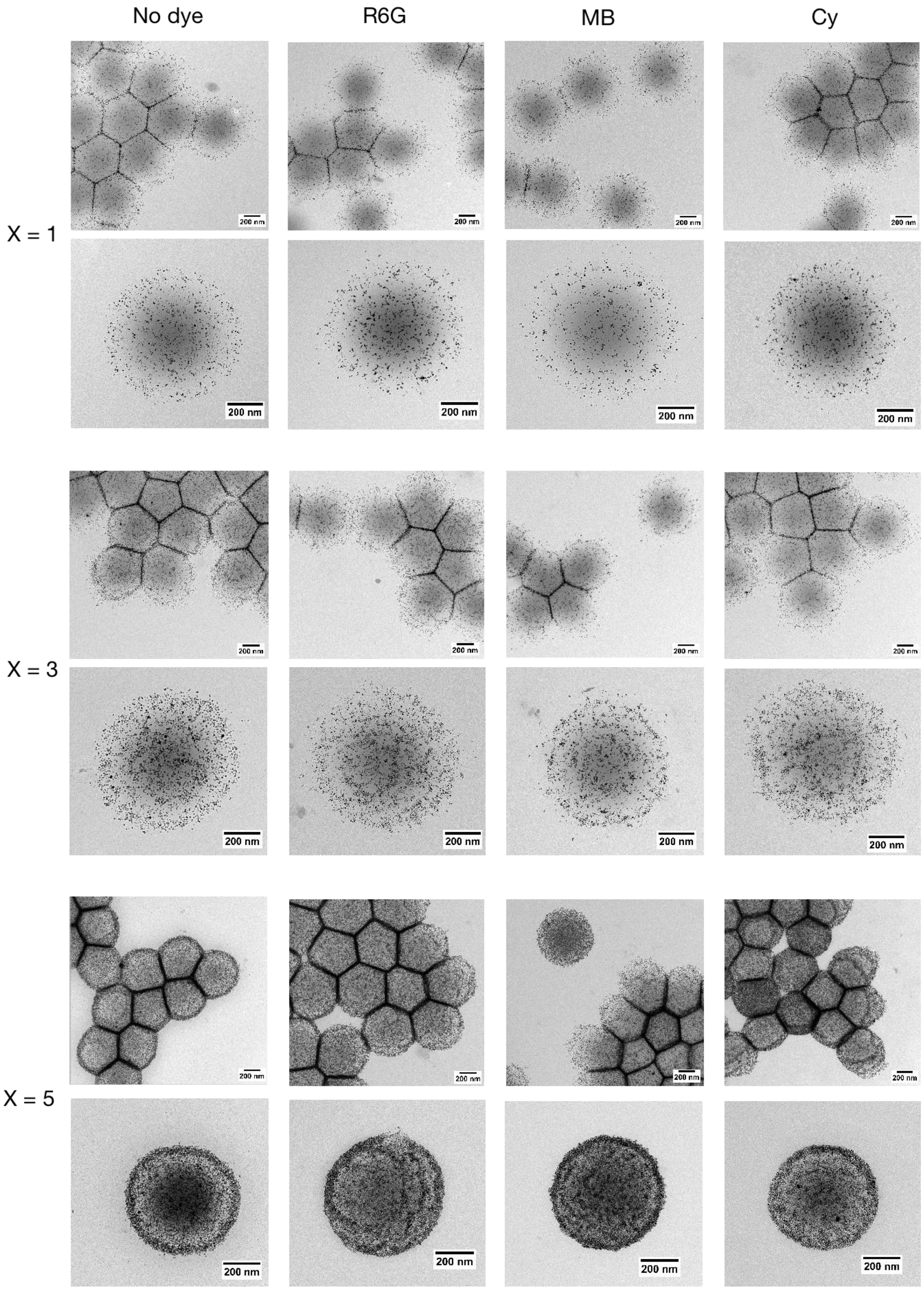

**Figure 3.** Typical TEM images of hybrid μGels obtained after incubation of bare (no dye) or Gel@dye particles with Au NPs. The number of incubation steps between the μGels and the Au NPs is specified on the left by the values of x, varying from 1 to 5. All the Gel@dye particles were prepared from $[\text{Dye}]_0$ = 50 μM at pH 7.5 and RT while the concentration of Au NPs was [AuNPs] = 0.27 $\mu\text{mol.L}^{-1}$.

The concentration of the Au NPs solution ([Au NPs] = 0.27 $\mu\text{mol.L}^{-1}$) used for the assembly process corresponds to the one obtained just after Au NPs synthesis. Due to their small size and high colloidal stability, it was not possible to concentrate further the Au NPs solution by centrifugation. Hence, the procedure consisting in performing several incubation steps (up to five times) with the same Au NPs solution, instead of concentrating the initial Au NPs solution, appeared as an attractive strategy to increase the loading of Au NPs within the Gel@dye samples. The excess of Au NPs (free Au NPs in solution) was removed by 1 cycle of centrifugation/redispersion in water and the supernatant was analyzed by UV−vis spectrophotometry to deduce the Au NPs uptake within the μGels ($\text{AuNPs}_{\text{uptake}}$) and loading efficiency (see Table 1). However, the $\text{AuNPs}_{\text{uptake}}$ values may be slightly overestimated as some Au NPs were found adsorbed on the centrifuge tubes after centrifugation, thus artificially decreasing the amount of free Au NPs measured in the supernatant. It is noteworthy that even in the absence of dyes, the μGels were able to load similar amounts of Au NPs (see Fig. 3), showing that the presence of cationic dyes within the μGels matrix is not the only parameter responsible for the large Au NPs uptake. The hybrids obtained from the three different dyes were named $\text{Gel@dye@Au}_{(x)}$, where *dye* stands for R6G, MB or Cy and x indicates the number of incubation steps between the μGel@dyes and the Au NPs solution (x = 1, 3 or 5).

## 2.2 Optical properties

The optical properties of $\text{Gel@dye@Au}_{(x)}$ were analyzed using UV-vis spectroscopy (Fig. 4). The plasmon band of Au NPs could be detected in the spectral range 510-560 nm while the presence of the dyes was revealed by absorption bands at 539 nm for R6G, 661 nm for MB and 808 nm for Cy. The uptake of Au NPs during the successive incubation steps with μGels could be monitored by following the plasmon band intensity, which strongly increased after x = 1, 3 and 5 incubation cycles. Depending on the amount of dyes and Au NPs uptaken by the μGels, the relative band intensities of each component appeared to vary strongly, revealing predominantly either the dye absorption bands (at high dye loading and low Au NPs uptake (x=1)) or the plasmon peak (for high Au NPs uptake (x=3 or 5)).

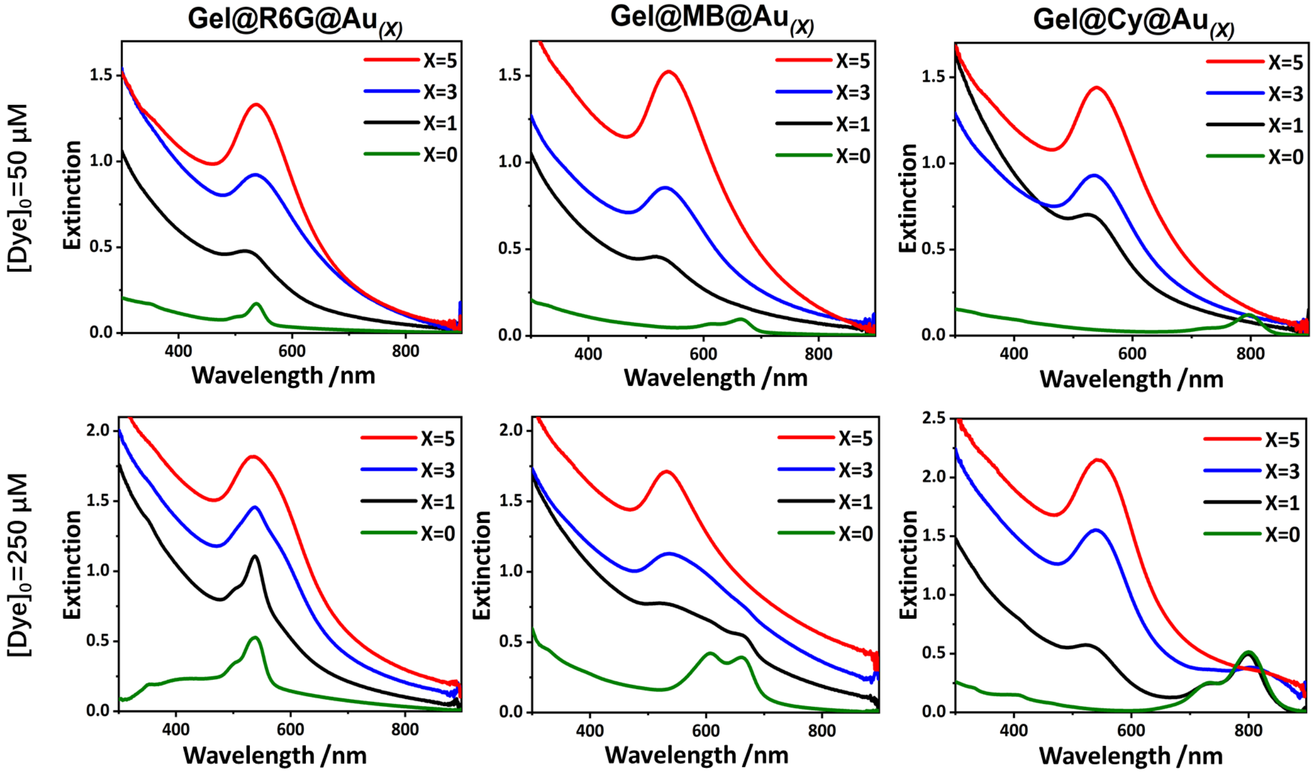

**Figure 4.** UV-vis spectra of aqueous solutions (pH 7.5) of Gel@dye and Gel@dye@Au$_{(x)}$, at 0.01 nM for an optical path length of 1 cm, with Dye = R6G, MB or Cy prepared from [Dye]$_0$ = 50 μM or 250 μM. Spectra were obtained before incubation with Au NPs (green curves) or after x = 1 incubation (black curves), 3 incubations (blue curves) or 5 incubation cycles (red curves).

### 2.3 Coarse-grained simulations of the mechanisms driving the assembly of the μGels, dyes and NPs

In order to get insight on the mechanism of Au NPs and dye uptake by μGels, coarse grained computer simulations[21, 22] were performed, based on the bead-spring model, considering the fluctuations of the polymer chains and the existence of nodes in the polymer networks. Monomeric units forming polyelectrolyte chains, nanoparticles and ions (including the dye molecules) were modelled as spheres whereas the solvent was considered as a dielectric continuum. The simulated μGels consisted in 100 polyelectrolyte chains of 15 monomeric units (diameter of 0.65 nm) connected by 66 crosslinkers. The most inner cross-linkers (40%) connected four polyelectrolyte chains and the external ones connected three or two chains. The resulting simulated gel particle displays an effective diameter of *ca.* 34 nm, which is one order of magnitude smaller than the size of the μGels in the experiments. However, larger gels would imply an unaffordable computational cost and we expect the mechanisms driving the absorption of dyes or nano-particles to be similar in nanogels or μGels. Diameters of 4.00, 1.00 and 0.70 nm were chosen for the nanoparticles, dyes and the rest of hydrated ions, respectively. The dyes were modelled as cationic species and the anions and cations in the medium as monovalent species. Nanoparticles were assumed to have an electric charge of $-4e$, corresponding to a zeta potential close to that of real NPs. The electrostatic potential of the nanogel was of the same order as that of the μGels: on average, the electric charge per chain was $-0.25e$ (where $e$ stands for the elementary charge) since one in four polyelectrolyte chains carried a charged anionic group. Simulations considered four types of interactions:

(i) Steric repulsion between constituents (monomeric units, ions, dye molecules or nanoparticles) due to excluded volume effects, modeled by means of the Weeks–Chandler–Andersen potential.

(ii) Elastic bonds between consecutive monomeric units, modeled through Hook's interaction potential.

(iii) Electrostatic forces between charged species, included through the Coulomb potential.

(iv) Van der Waals interaction between the monomeric units and the nanoparticles or the dye molecules.

The potential energy ($u(r)$) of these forces is given by $u(r) = -B_{mi}/r^6$, where $B_{mi}$ is the dispersion constant for monomeric units and species $i$, which can be nanoparticle ($B_{mn}$) or dye ($B_{md}$), and $r$ is the center-to-center distance between two given interacting particles, as described in previous works[21, 22]. Hereafter, the values of $B_{mn}/k_BT$ and $B_{md}/k_BT$ (where $k_B$ is Boltzmann's constant and $T$ is the absolute temperature) are expressed in nm$^{-6}$.

As shown in the typical snapshots of simulated systems in Figure 5, nanoparticles remain outside the nanogel (Fig. 5a) at low Au NP concentration and in the absence of dyes. When the Au NP concentration increases in the medium, the loading of NPs in the nanogel becomes possible (Fig. 5b). Nanoparticles diffuse from the external medium to the interior of the nanogel due to the difference of concentrations, as hypothesized in E. Cazares-Cortes et *al*[9]. Interestingly, in the presence of dyes, the uptake of NPs is feasible even at low NP concentrations (Fig. 5c), indicating that another mechanism is involved. Based on the simulation results, the presence of attractive Van der Waals forces between the dyes and the nanogel (see Fig. S2) would promote the uptake of dyes. In this case, NP loading would be also electrostatically driven due to the attractive interactions between the negatively charged NPs and cationic dye-loaded nanogel, although this effect is probably weak in our experiments as the zeta potential values of the μGels hardly changes after the loading of the dyes (see above, section 2.1). Altogether the simulation highlights the key roles of (i) the concentration gradient fostering diffusion of NPs within the gel, independently of the presence of dyes, and (ii) the attractive forces (Van der Waals and electrostatic interactions) promoting the loading of the cationic dyes and resulting in NP uptake.

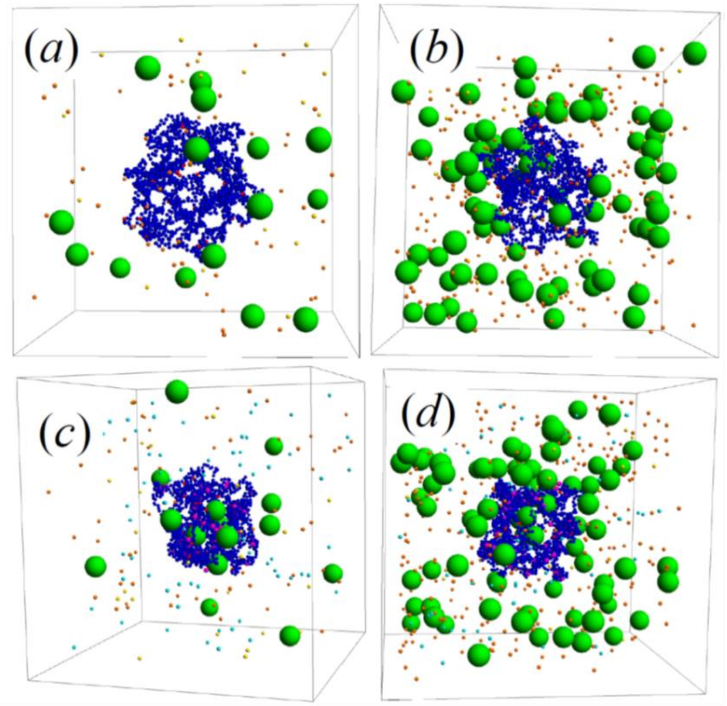

**Figure 5.** Snapshots of the simulation cell for: a) [Au NP] = 0.2 mM, [Dyes] = 0 M; b) [Au NP] = 1.0 mM, [Dyes] = 0 M; c) [Au NP] = 0.2 mM, [Dyes] = 1 mM, $B_{md}/k_BT$ = 0.75 nm$^{-6}$; d) [Au NP] = 1.0 mM, [Dyes] = 1 mM, $B_{md}/k_BT$ = 1.00 nm$^{-6}$. Blue and red beads represent neutral and charged monomeric units of the nanogel, respectively. Green and magenta beads stand for nanoparticles and dye molecules. Yellow, orange and cyan beads represent counterions corresponding to the nanogel, the nanoparticles and the dyes, respectively.

## 2.4 Stimuli-responsive properties

The stimuli-responsive properties of bare and hybrid μGels were studied using DLS, by analyzing the swelling-deswelling behavior induced by temperature or pH changes. The pH was varied in steps of 0.5 over a range from 2 to 10 while the temperature was changed from 10°C to 70°C (Fig. 6, the corresponding data are provided in Tables S1 and S2). For all samples, $D_h$ was observed to decrease sharply as the temperature increases, emphasizing their thermoresponsive response. The inflection points observed in the curves of $D_h$ *vs* temperature were used to estimate the volume phase transition temperature (VPTT). Below VPTT, interactions between the hydrophilic segments of the polymer network and water molecules are favored, with the formation of hydrogen bonds, resulting in the swelling of the μGels.

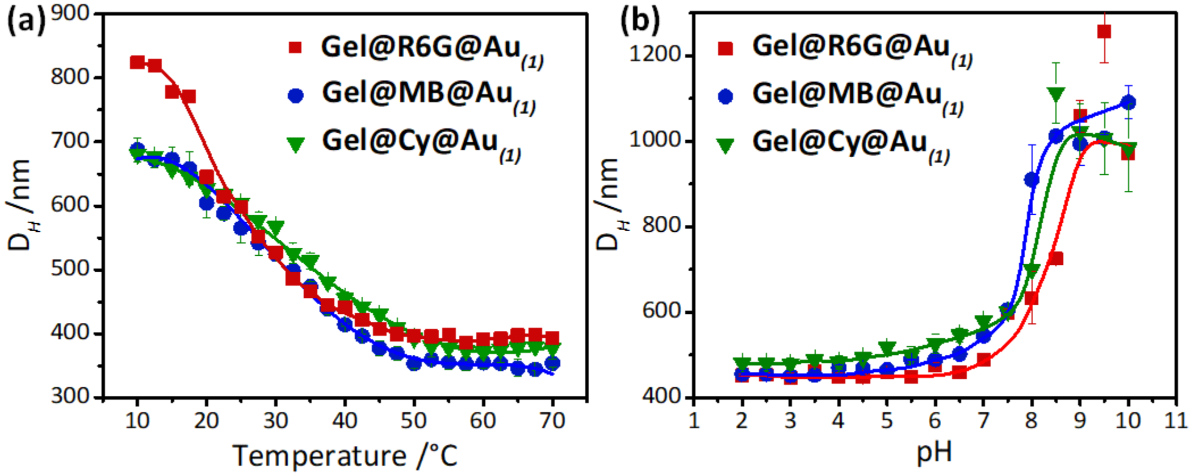

**Figure 6.** Plots of $D_H$ determined by DLS *vs* temperature (at pH 7) (a) and *vs* pH (at 25 °C) (b) for Gel@R6G@Au$_{(1)}$ (squares), Gel@MB@Au$_{(1)}$ (circles) and Gel@Cy@Au$_{(1)}$ (down triangles) hybrid μGels. All Gel@dye@Au$_{(1)}$ samples were prepared from $[Dye]_0$ = 50 μM, after x = 1 incubation cycle with Au NPs solution ([AuNPs] = 0.27 μmol.L$^{-1}$). The lines were added for the sake of clarity but have no physical significance. (a) and (b) were measured with two different batches.

When the temperature increases above VPTT, water-polymer interactions are reduced due to hydrogen bond disruption while interactions between the hydrophobic portions of the polymer increase, leading to dehydration and self-aggregation of polymer chains, thus collapsing the microgel matrix and expelling water. The VPTT was found to be ~ 30°C for the hybrid particles, smaller than the VPTT of bare μGels (*ca.* 50°C)[6,7], indicating that the loading of dyes and Au NPs modifies the hydrophilic/hydrophobic balance of the hydrogel matrix. The reversibility of the temperature-induced swelling-deswelling behavior was assessed on Gel@Cy@Au$_{(1)}$ samples by cooling down the solution after the heating cycle. As observed in Fig. S3, the hydrodynamic size of the hybrid μGels increases when the temperature decreases, returning back to its initial value, confirming the reversible character of the phase transition. From the $D_h$ values recorded at 20°C and 60°C, the maximum swelling ratio $\alpha_{max}$ could be calculated, according to eq. 3.

$$\alpha_{max} = \frac{V_{swollen}}{V_{collapsed}} = \frac{R^3_{h,swollen}}{R^3_{h,collapsed}} \qquad \text{(eq. 3)}$$

$\alpha_{max}$ characterizes the maximum amount of water that can be loaded and released by the μGels. As shown in Table 2, a clear enhancement of the swelling/deswelling capacity of the hybrid networks is observed, compared to the pristine μGels.

**Table 2.** Characteristics of pristine and hybrid μgels at pH 7 determined from DLS and zeta potential measurements. All Gel@dye@Au$_{(1)}$ samples used for the Table below were prepared from $[Dye]_0$ = 50 μM, after x = 1 incubation cycle with Au NPs solution ([Au NPs] = 0.27 μmol.L$^{-1}$).

| ***Samples*** | *$D_h$ at 20°C nm (PDI)* | *$D_h$ at 60°C nm (PDI)* | ***ζ (mV)*** | $\alpha_{max}$ |
|---|---|---|---|---|
| Bare μGel | 592 ± 11 (0.11) | 396 ± 4 (0.25) | -21.7 | 3.3 |
| Gel@R6G@Au$_{(1)}$ | 670 ± 20 (0.20) | 391 ± 4 (0.18) | -23.2 | 5.0 |
| Gel@MB@Au$_{(1)}$ | 604 ± 2 (0.20) | 354 ± 8 (0.16) | -22.4 | 5.0 |
| Gel@Cy@Au$_{(1)}$ | 627 ± 2 (0.12) | 372 ± 6 (0.02) | -20.8 | 4.8 |

The μGels turned out to be concomitantly pH responsive. Indeed, raising the pH value from 2 to 10 resulted in a strong increase of $D_h$ with a transition observed in the range 6-9 (see Fig. 6b). This pH-sensitive behavior can be explained on the basis of the Flory–Rehner theory[26, 27], in which the equilibrium swelling state of hydrogel networks is achieved when the total osmotic pressure $\Pi_T$ tends towards 0. $\Pi_T$ can be calculated by summing up the mixing ($\Pi_{mix}$), elastic ($\Pi_{el}$) and ionic ($\Pi_{ion}$) contributions ($\Pi_T = (\Pi_{mix} + \Pi_{el} + \Pi_{ion})$ [28]. When the pH increases above the $pK_a$ of carboxylic acid groups, their ionization rises the internal osmotic pressure due to electrostatic repulsions and free counterion motion, resulting in further swelling.

The UV-vis spectra of Gel@dye@Au$_{(x)}$ samples were recorded at two different temperatures (25 and 60°C) to reveal the influence of this stimulus upon the optical properties of the hybrid particles (Fig. 7). As can be observed in Fig. 7a, an increase in temperature, from 25 to 60°C, had almost no effect on the shape of the plasmon band for the Gel@dye@Au$_{(1)}$ samples, reflecting the absence of plasmonic coupling between Au NPs within the μGels matrix. This can be explained by the low density of Au NPs which are individually dispersed and isolated within the hydrogel matrix, even after temperature-induced particle shrinking. In contrast, as the uptake of Au NPs increases within Gel@dye@Au$_{(3)}$ and Gel@dye@Au$_{(5)}$, their heating results in a broadening and a red shift of the plasmon band which is much more pronounced for the μGels containing a high loading of Au NPs. In this case, the huge density of Au NPs trapped inside the μGels likely results in a short distance between them, which is even shorter once the μGels have shrunk upon heating, leading to plasmonic coupling. These temperature-induced optical changes appear to be only partly reversible, which can be explained by the irreversible character of Au NP aggregation, due to strong van der Waals attraction between them. The effect of pH was also studied by recording the UV-vis spectra of the hybrid particles at pH 5.5 and 7.5. These pH values were selected to mimic both the physiological pH (7.4) and intracellular lysosomal pH (around 5.5). As observed in Fig. 7b, the decrease in pH from 7.5 to 5.5 produced a broadening of the plasmon band, which can be explained by the presence of plasmonic coupling between NPs within the μGels. This effect was much less pronounced than for the temperature stimulus, probably due to the choice of the pH range which lies at the bottom of the pH-induced volume-phase transition (see Fig. 6b). Nevertheless, a significant enhancement of the absorbance in the NIR region could be observed at pH 5.5 for Gel@dye@Au*(3-5)* samples, which is a key point for potential biomedical applications. Interestingly, the combination of the two stimuli (temperature and pH changes) appeared to further enhance the modifications of the plasmon band shape and wavelength, as observed in Fig. 7c. These results thus show that the presence of dyes and Au NPs trapped within the microgels do not prevent the conformational changes of the copolymer network, which retain its stimuli-responsive properties.

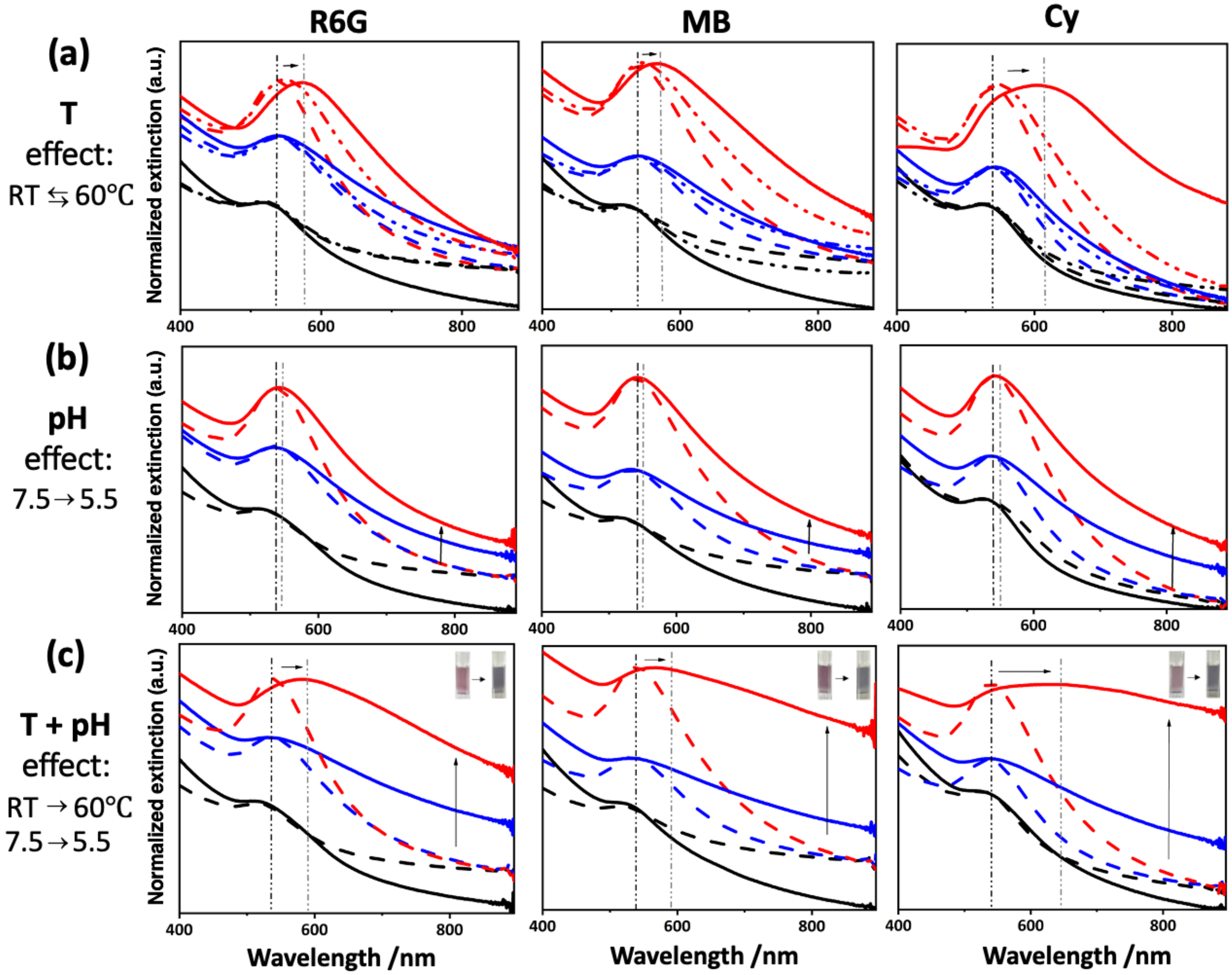

**Figure 7.** Effect of temperature and pH stimuli upon the UV-vis spectra of Gel@dye@Au*(x)* samples at 0.01 nM, with dye = R6G, MB or Cy ([Dye]$_0$ = 50 μM). The number of incubation steps between μGels and Au NPs was

varied from x = 1 (black curves), to x = 3 (blue curves) and x = 5 (red curves). For each value of x (1-5), the spectra were normalized relative to the ones recorded at room temperature (RT) and pH 7.5 (dashed lines). (a) UV-vis spectra as a function of temperature: the full lines correspond to the spectra recorded at 60 °C and the dashed-dotted lines are the spectra after cooling down. (b) UV-vis spectra as a function of pH: the full lines correspond to the spectra recorded at pH 5.5. (c) Influence of both stimuli, *i.e.* temperature and pH: the full lines correspond to the spectra recorded at pH 5.5 at 60°C. The insets display the optical pictures of the Gel@dye@Au$_{(5)}$ solutions before and after triggering the stimuli.

The morphology changes of Gel@dye@Au$_{(5)}$ samples induced by pH and temperature stimuli were observed by TEM (see Fig. 8). A temperature increase from RT to 60°C appears to induce both (i) a μGel shrinkage with an overall decrease in diameter and (ii) the aggregation of Au NPs within the polymer network. Regarding the pH stimulus, a decrease in pH from 7.5 to 5.5 has much less effect on the size of the μGels, which is consistent with the DLS measurements but it induces a clear aggregation of the Au NPs. Interestingly, the combination of these two stimuli further amplifies these morphological modifications (μGel collapse and Au NPs aggregation).

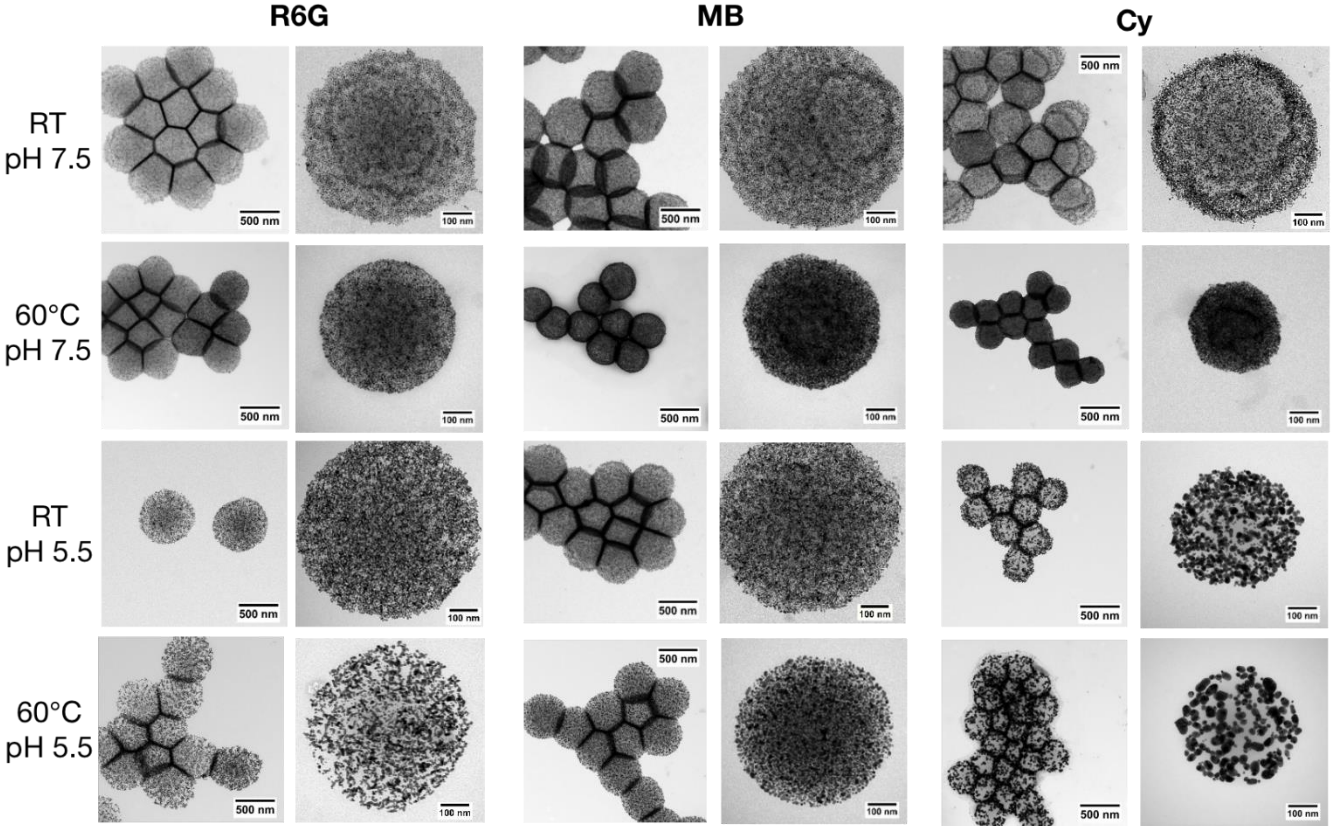

**Figure 8.** TEM images at different magnifications of Gel@dye@Au$_{(5)}$ samples prepared from [Dye]$_0$ = 50 μM, recorded initially at room temperature (RT) and pH 7.5 and then submitted to different stimuli. The effect of temperature (T) corresponds to the heating of the colloidal dispersions to 60°C, the effect of pH corresponds to the decrease of pH to 5.5 while the effect of temperature and pH indicates that the hybrid particles were subject to both stimuli simultaneously.

The structure of the μGels loaded with the different dyes (R6G, MB, Cy at $[\text{dye}]_0$ = 50 μM) and Au NPs (x =1 or 5) has been studied by synchrotron small angle X-ray scattering (SAXS) on the SOLEIL/SWING beamline. This non-denaturing method allowed us to characterize the structure of the μGels and NPs on several length scales (*i.e.* 1-300 nm, Fig. 9). We recall that the intensity scattered by an assembly of spheres of volume V depends on their average size through the sphere form factor P(q) and their organization through the average structure factor S(q) as follows:

$$I(q) = \Phi . V . (\Delta\rho)^2 . P(q) . S(q) \qquad \text{(eq. 4)}$$

where $\Phi$ is the volume fraction of the particles, q is the norm of the scattering vector and $\Delta\rho = \rho_{sphere} - \rho_{water}$ is the contrast of X-ray scattering length density (ρ) between the spheres and water.

We first considered reference suspensions composed purely of μGels or Au NPs. The scattering curve of μGel suspension (*i.e.* x = 0, Figure 9a) exhibits oscillations at low q (i.e. $q < 0.01$ Å$^{-1}$) which correspond fairly well to the form factor of non-interacting (i.e. $S(q) = 1$) polydisperse spheres with a mean diameter D = 500 nm and a log. normal size distribution (polydispersity: σ = 0.05). This analysis agrees with the DLS result (*i.e.* $D_h$ = 592 nm) considering that our SAXS measurement should underestimate the contribution of dangling chains on the surface of μGels compared to DLS measurements. The scattering curve of Au NP suspension (Figure 9b) differs clearly from the μGel curve by the absence of oscillations at small q and a decay at large q corresponding to the sphere form factor of polydisperse spheres with a mean diameter D ≈ 3.3 nm and log. normal polydispersity (*i.e.* σ = 0.4).

We then characterized the different types of μGels loaded with dyes and Au NPs at two different pH (Figure 9c, 9e,9g). Overall, all the scattering curves have the same shape. At low q (i.e. $q < 0.01$ Å$^{-1}$), the scattered signal is dominated by the well-defined oscillation series corresponding to the contribution of the μGel beads while at high q (i.e. $q > 0.03$ Å$^{-1}$) the scattered signal is dominated by the contribution of the NPs.

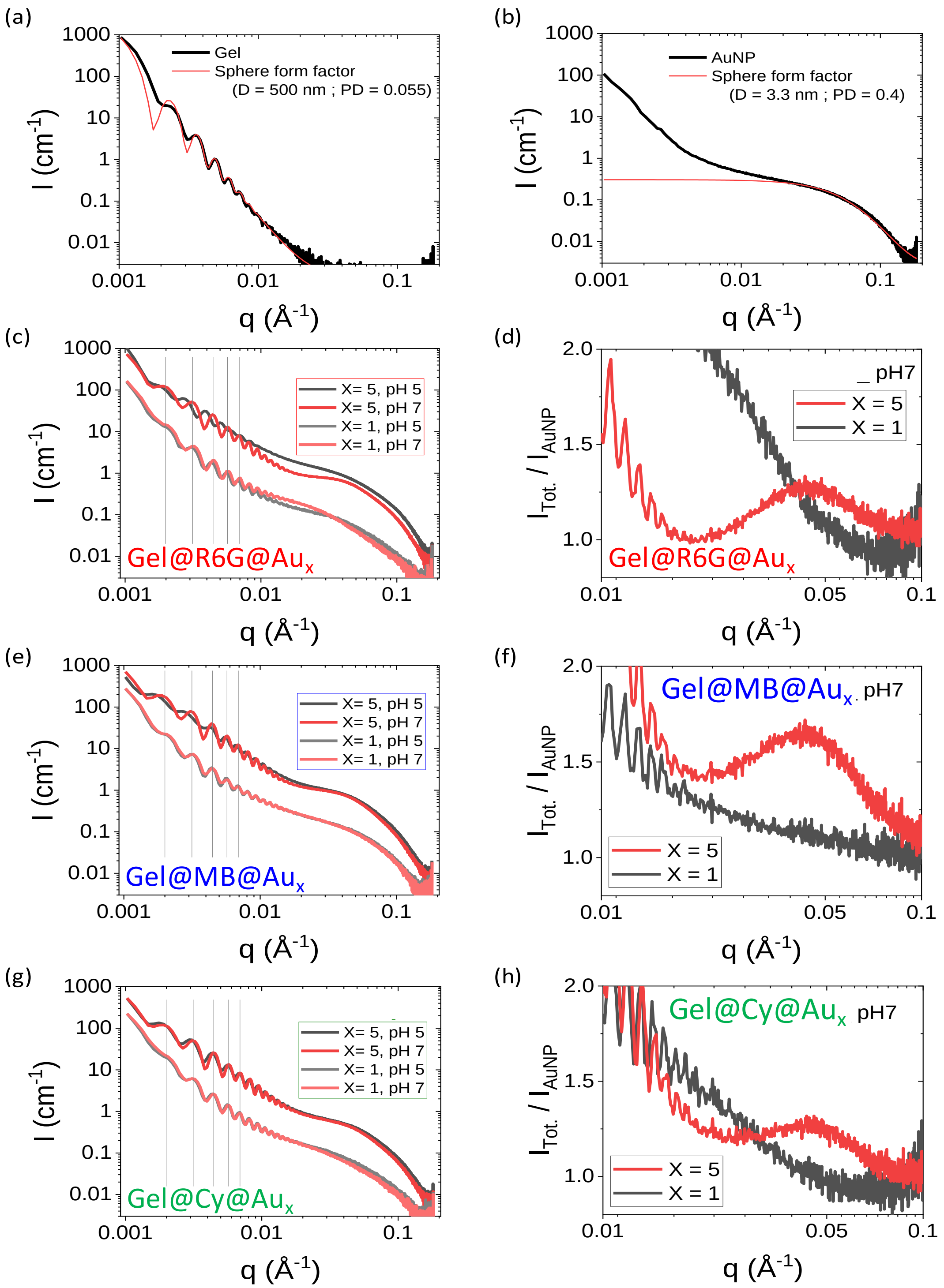

**Figure 9.** Small angle X-ray scattering (SAXS) patterns of aqueous solutions (pH = 7 or 5) of (a) µGels, (b) Au NPs and (c, e, g) Gel@dye@Au$_{(x)}$, with dye = R6G, MB or Cy and x = 1 or 5. All measurements were done at room temperature. Figures d, f and h represent the ratio between the total intensity ($I_{Tot.}$(q)) scattered by the suspension of Gel@dye@Au$_{(x)}$ and the intensity scattered by a suspension of Au NPs at the same concentration ($I_{AuNP}$ (q)) as a function of q at pH 7. The curves corresponding to pH 5 are available in SI (Fig. S4).

As expected, the analysis of the high q domain shows that the size and polydispersity of Au NPs is the same in all cases and corresponds to the result obtained for a suspension of free Au NPs. Knowing the average size of Au NPs, one can exploit the fact of working in absolute units to calculate their concentration in the medium, using the following expression: $c = \frac{I(q \to 0)\rho^2 N_A}{M_w(\widetilde{\rho_P} - \widetilde{\rho_0})^2}$ with the gold volumic mass $\rho \approx 19.3\ g/cm^3$, the Avogadro number $N_A \approx 6.022 \times 10^{23}$ $mol^{-1}$, the molecular mass of Au NPs $M_w \approx 200\ k$g/mol, the difference of X-Ray scattering length density between Au NPs ($\widetilde{\rho_P}$) and water ($\widetilde{\rho_0}$): $\widetilde{\rho_P} - \widetilde{\rho_0} \approx (130 - 9.46) \times 10^{10}\ cm^{-2}$. It appears that the concentration increases on average by a factor of 5 when x (number of incubation steps between the μGels and the Au NPs) increases from 1 to 5 (see Table 3), demonstrating the possibility to finely tune the amount of Au NPs loaded within the μGels via the number of incubation steps. Another significant effect related to the increase of x concerns the local organization of Au NPs. This effect is highlighted by plotting the ratio between the total intensity scattered by the suspension of Gel@dye@Au ($I_{Tot.}$(q)) and the intensity scattered by a suspension of Au NPs at the same concentration ($I_{AuNP}$ (q)) (Figure 9d, 9f, 9h). At high q (*i.e.* q > 0.03 $Å^{-1}$), this ratio corresponds to the structure factor S(q) of the NPs inside the μGels. As shown on Figure 9d, 9f, 9h, the increase of x from 1 to 5 leads to the appearance of a structure peak revealing a correlation distance between Au NPs. Interestingly, this peak tends to widen and the position of the peak maximum (q*) shifts towards the large q as the pH decreases, such as: q* ≈ 0.035 $Å^{-1}$ at pH 7 and q* ≈ 0.05 $Å^{-1}$ at pH 5. This shift reflects a decrease in the average interparticle distance (edge-to-edge) from 14 nm to 9 nm, in qualitative agreement with the result of UV-vis spectroscopy showing an amplification of the plasmonic coupling with a decrease of pH.

Finally, we analyzed the low q domain to characterize the behavior of the μGels in the different conditions. This analysis shows that the scattering curves are almost superposable in all cases (Figures 9c, 9e and 9g) with diameters around 560 nm. Thus the size variation detected by DLS and suggested by the evolution of the structure peak for x = 5 does not appear significantly in our analysis. This counter intuitive result may be explained by the fact that the μGel structure is heterogeneous and reorganizes with pH without apparent modification of the scattering curves at low q.

**Table 3.** Au NP mass concentrations in Gel@dye@Au$_{(x\,=\,1\text{ or }5)}$ samples determined from the SAXS measurements shown in Figure 9.

| **Samples** | **pH = 5** | | **pH = 7** | |
|---|---|---|---|---|
| | **x = 1** | **x = 5** | **x = 1** | **x = 5** |
| Gel@R6G@Au$_{(x)}$ | 0.08 g.L$^{-1}$ | 1.01 g.L$^{-1}$ | 0.11 g.L$^{-1}$ | 0.55 g.L$^{-1}$ |
| Gel@MB@Au$_{(x)}$ | 0.16 g.L$^{-1}$ | 0.88 g.L$^{-1}$ | 0.17 g.L$^{-1}$ | 0.94 g.L$^{-1}$ |
| Gel@Cy@Au$_{(x)}$ | 0.10 g.L$^{-1}$ | 0.56 g.L$^{-1}$ | 0.09 g.L$^{-1}$ | 0.50 g.L$^{-1}$ |

## 2.5 Photothermal properties

To assess the photothermal performances of Gel@dye@Au$_{(x=1\text{ or }5)}$, the temperature changes of particle dispersions under illumination were recorded using a thermal imaging near infrared camera (Fig. 10). The illumination was performed with a 808 nm laser at power densities of 1.1 W.cm$^{-2}$ and the temperature was measured for 300 s. The heating profiles were investigated on 100 μL of particle dispersions at fixed μGel (1.73 mg.mL$^{-1}$) and dye concentration (2.8-2.9 μmol of dyes per g of μGels, which corresponds to [Dye]$_0$ = 50 μM in Table 1) but different Au NPs loading (x = 0, 1 or 5). Illumination of the dye-loaded μGels with no Au NPs trapped inside their matrix, did not result in any appreciable temperature variation, except for Gel@Cy which exhibits a small temperature increase ($\Delta T = 2$ °C) within the first 25 s, likely due to Cy absorption at this laser excitation. This slight temperature increase is followed by a fast decline that can be explained by the well-known photo-instability of Cy[29], for which the main photobleaching pathway has been shown to be initiated by its triplet state that sensitizes oxygen resulting in the formation of singlet oxygen [30]. In the presence of Au NPs loaded within the gels, the suspensions showed a more significant time-dependent increase in temperature (Fig. 10), due to the photothermal properties of Au NPs in dye-loaded μGels, converting light into heat. As expected, the heat release appeared much higher for densely loaded µGels (Gel@dye@Au$_{(5)}$) with ΔT values over 20 °C than for weakly doped µGels (Gel@dye@Au$_{(1)}$), showing ΔT values of *ca.* 2-5 °C.

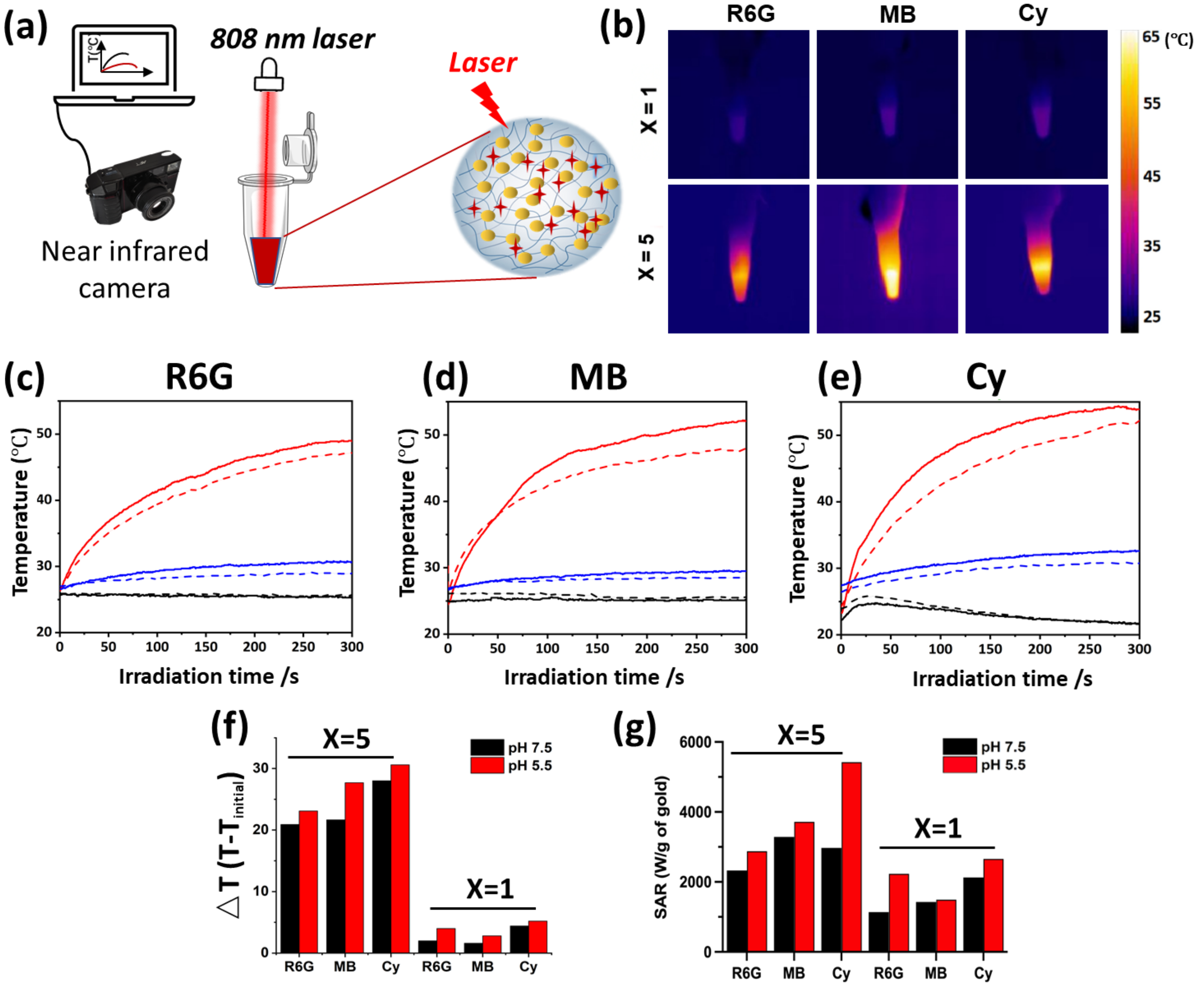

**Figure 10.** Heating properties of Gel@dye@Au$_{(x=0,\ 1\ or\ 5)}$ suspensions at 0.04 nM exposed to a 808 nm laser at 1.1W/cm$^2$. (a) Illustration of the experimental setup, (b) Pictures of the suspensions exposed to the laser and monitoring of the heating by an infrared camera, (c-e) Heating profile of Gel@dye@Au$_{(x)}$ at different pH. The plain lines correspond to pH 5.5 while the dashed lines correspond to pH 7.5. The colors of the lines correspond to: x=0, *i.e.* no Au NPs (black lines), x=1 (blue lines), x=5 (red lines), (f) Temperature increment after irradiation for 300 s for the different Gel@dye@Au$_{(x=1\ or\ 5)}$ at pH 5.5 and pH 7.5, (g) Corresponding SAR values for the different Gel@dye@Au$_{(x=1\ or\ 5)}$ at pH 5.5 and pH 7.5.

Interestingly, the enhancement of the heating capacities of Gel@dye@Au$_{(5)}$ compared to Gel@dye@Au$_{(1)}$ was higher than expected and could not be only related to the higher number of Au NPs within the µGel matrix. Indeed, the ΔT values were 6 to 10 times higher for densely filled µGels (x = 5) while the amount of Au NPs was no more than 5 times higher. To compare quantitatively the heating power of the different µGels, the specific absorption rate (SAR, in W/g of materials) was calculated, taking into account the mass of gold for the normalization. The SAR values are reported in Fig. 10g, confirming that for a given mass of gold, the SAR indeed increased with the Au NPs loading within the µGels and with the decrease of pH to 5. This effect is particularly pronounced for the Cy-containing µGels. The superior heating capacities of Gel@dye@Au$_{(5)}$ could be explained by the presence of strong electromagnetic coupling between Au NPs at high loading, generating hot spots as suggested by the stronger interactions between Au NPs revealed by SAXS and observed on TEM pictures of µGels as well as coupling between the Cy dye and Au NPs. Additionally, the gradual shrinking of the µGels with temperature enhances the optical attenuation. A further improvement of the heating capacities of Gel@dye@Au$_{(5)}$ was observed by lowering the pH from 7.5 to 5.5, probably due to enhanced plasmon coupling of Au NPs and of Au NPs and dye within the µGels, consistent with the UV-vis spectra at pH 5.5 (cf. Fig. 7).

### 2.6 Viability assay, cellular uptake, and phototoxicity in colon carcinoma cells

In order to assess the usability and behavior of such smart stimulable µGels upon cellular internalization, we first investigated the effect of Gel@dye@Au$_{(x)}$ samples on the viability of CT26 colon carcinoma cell lines by measuring their metabolic activity using the Alamar Blue assay. Cells were incubated for 24 hours in a complete medium containing Gel@dye@Au$_{(1\text{ or }5)}$ (see details of the experiments in supporting information part 1.6). To compare the effect of the hybrid particles to that of the free dyes, cells were also incubated with the same dye concentrations as the one loaded within the µGels (final dye concentrations in the cell culture medium of 5 µM and 25 µM, respectively, for the Gel@dye@Au$_{(1\text{ or }5)}$ samples prepared from either [Dye]$_0$ = 50 µM or 250 µM). As observed in Fig. 11, at these concentrations, free R6G and

MB exhibit a high cytotoxicity, in line with previously published studies[31, 32, 33], with only 30% and 20 % of cell viability respectively, at 5 µM and less than 10 % at 25 µM.

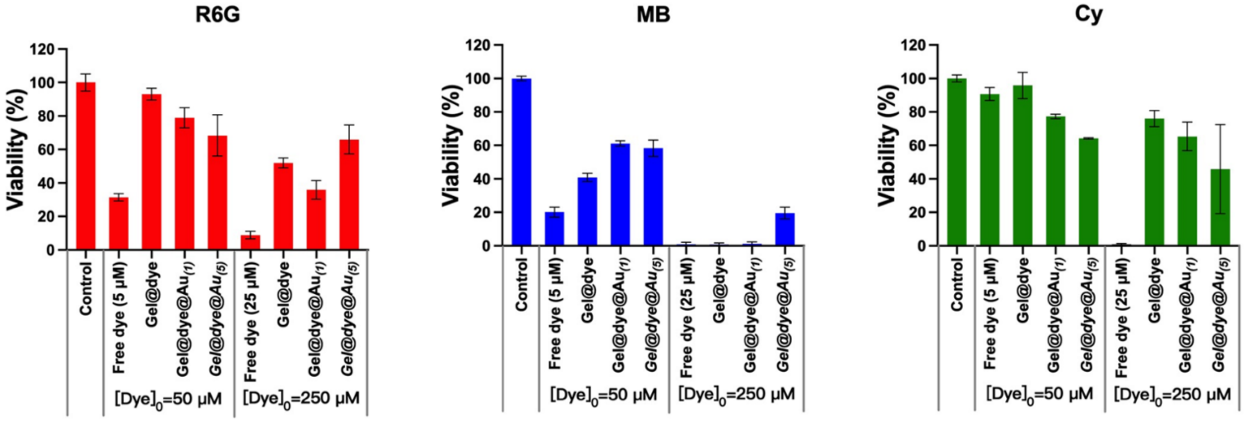

**Figure 11.** Viability of CT 26 cells tested by Alamar Blue assay after 24 h of incubation with free dyes, Gel@dye or Gel@dye@Au samples prepared from $[Dye]_0$ = 50 µM or 250 µM with Dye = R6G, MB or Cy and Au NPs (x=1 and 5). For the $Gel@dye@Au_{(1 \text{ or } 5)}$ samples prepared from either $[dye]_0$ = 50 µM or 250 µM, the final dye concentrations in the cell culture medium are 5 µM and 25 µM, respectively.

Cy appears toxic also but less than the other dyes at 5 µM with 90 % viability while it falls to almost 0% at 25 µM. Interestingly, after their uptake by the µGels, the dyes displayed much lower toxicity than in the free state, at equivalent concentrations. Such lower toxicity might be due to different internalization pathway and intracellular release when the dyes are vectorized by the µGels. To better understand the fate of the µGels upon interactions with tumor cells, cell were observed by laser confocal microscopy at different incubation times with the $Gel@dye@Au_{(1)}$ and $Gel@dye@Au_{(5)}$ prepared from either $[dye]_0$ = 50 µM (Figure 12) or $[dye]_0$ = 250 µM (supplementary Fig. S5). The characteristic fluorescence of each dyes could be observed in cells, with progressive increase of intracellular fluorescence. Therefore, despite a certain degree of aggregation of the dyes within the µGels, detected at high concentration (particularly for Gel@MB, see UV-vis spectra in Fig. 2b) which may affect their fluorescence properties, their signals are intense enough to enable them to act as fluorescence tracers to visualize the µGel uptake and fate upon interaction with cells. After 5 min (0 h), no fluorescence is associated to cells. After 6 h of incubation, most of the cells show fluorescence with a cytoplasmic and perinuclear localization and the fluorescence intensity increases after 24 h of incubation for R6G and MB, whereas it tends to saturate at 24 h for Cy. A similar behavior was observed with µGels with the highest dye concentration (Fig. S5).

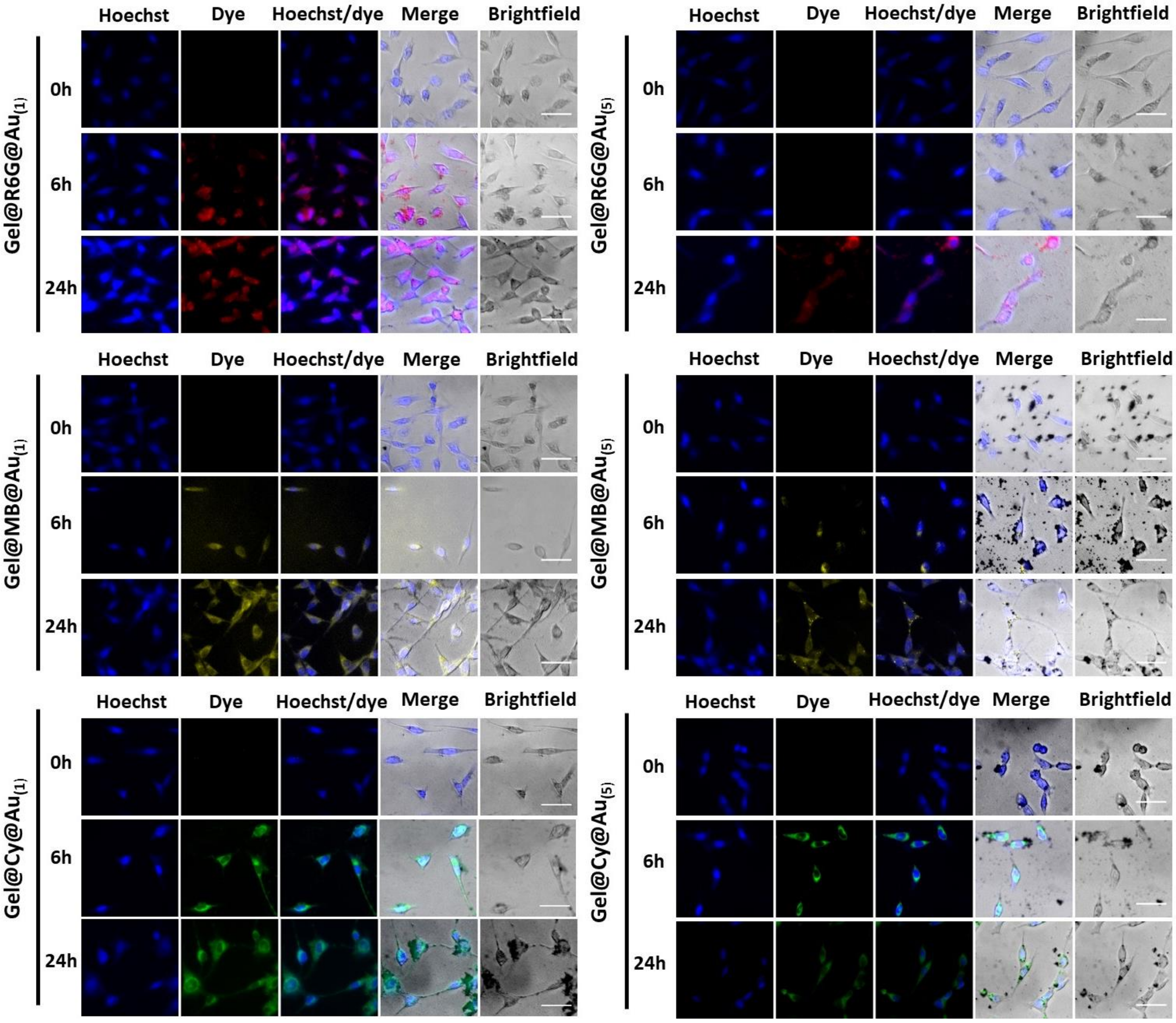

**Figure 12.** Bright field and fluorescence microscopy of CT26 cells incubated for 24 h with Gel@dye@Au$_{(1\ \text{or}\ 5)}$, ([Dye]$_0$ = 50 µM). After washing to remove µGels in excess, CT26 cells were further incubated for t=0, 6 h and 24 h and observed by HCS CellInsight CX7. Scale bar = 50 µm.

This suggests a time dependent uptake of µGels consistent with the process of endocytosis of sub-micrometer hydrogels. Note that at x=5, the aggregation of Gel@dye@Au$_{(5)}$ can be observed on bright field images, featuring dark spots outside (at 6 h, particularly for MB) and inside the cells (particularly at 24 h) showing simultaneous gold nanoparticle uptake. The fluorescence of the dyes is not associated with the dark spots when they are located outside the cells, probably due to fluorescence quenching whereas it becomes apparent inside the cells, likely due to the release of the dyes from the hybrid µGels or segregation of dye and Au NPs once inside the cells. Intracellular dye leakage could explain the dark toxicity of the hybrid µGels (Fig. 11), which is however less pronounced than the dark toxicity of the free dye. This study confirms the cellular uptake of hybrid µGels despite their large size, in agreement with previous works on alginate [34] and **[R2-3]** PNIPAM-based microgels[35] or polystyrene beads[36], which showed an internalization of large particles, although smaller particle size was correlated with greater extent of uptake. We further investigated the photothermal effect of Gel@dye@Au$_{(x)}$ on the viability of CT26 tumor cells. Due to the observed toxicity of samples loaded with high dye concentrations, we only focused in this study on the lowest dye concentrations for hydrogel loading ($[dye]_0$ = 50 µM). Monolayers of attached cells, previously incubated during 24 h with Gel@dye@Au$_{(x)}$ and rinsed, were irradiated for 10 min using 808 nm laser (power 1 and 2W/cm$^2$). The control experiments were performed on CT26 cells, without incubation with the µGel samples but irradiated with the same laser fluence. As shown in Figure 13, no cytotoxicity was observed with laser only. In line with dark toxicity study, cell treatment with Gel@Dye@Au$_{(x=1 \text{ or } 5)}$ (prepared from $[dye]_0$ = 50 µM) reduced cell viability to approximately 80% for x=1 and 70% for x=5 when no laser was applied (0 W/cm$^2$). After irradiation, the cell viability decreased drastically. The phototoxicity is increased with laser power (1 and 2 W/cm$^2$) and with Au NPs loading (x=1 or 5) in a dose dependant manner. Under optimal conditions (x=5, power of 2 W/cm$^2$), cell viability is only 40% for R6G, 30% for MB and 15% for Cy. The fact that Gel@Cy@Au$_{(5)}$ produces the highest cell death after laser irradiation is consistent with their absorbance signal in the near infrared region, which combines the absorption of the cyanine and Au NPs.

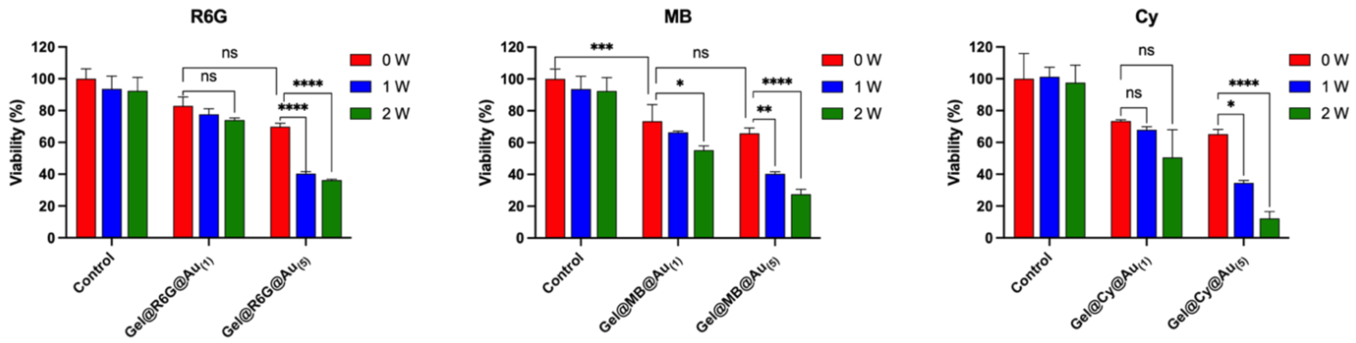

**Figure 13.** Phototoxicity of Gel@dye@Au$_{(1\ or\ 5)}$ measured by Alamar Blue assay on CT26 cells after 10 min irradiation at 808 nm laser at 1 and $2W/cm^2$. The results are shown as mean ± SEM（n=3). Two-way ANOVA for the analysis, ****p-value ＜0.0001, ***p-value ＜0.001, **p-value＜0.01, *p-value＜0.1 and ns represent no significant difference.

The absorbance is probably further increased by the effect of the low pH related to lysosomal uptake of the µGels and of the local increase of temperature. Interestingly the µGels with methylene blue induces an important cell death which might not be directly related to light-to-heat conversion at 808 nm. Dhaval Sanchala et al. explains the anticancer activity of methylene blue via the inhibition of Heat Shock Protein 70 (HSP70)[37]. Such effect could participate to the high phototoxicity induced by Gel@MB@Au$_{(1)}$ irradiated with NIR laser since MB could diminish the HSP 70 cell defense mechanism against thermal stress. An extensive study (going beyond the focus of the present paper) is underway to investigate the intracellular fate and optical properties of µGels with tunable Au NPs load and plasmon coupling in cells: we expect the lysosomal acidic pH, on one part, and photothermal effect, on the other part, to transform the intracellular structures of µGels and to result in interesting therapeutic and sensing applications. Here we have shown that the Gel@dye@Au$_{(1\ or\ 5)}$ could induce massive cell death when irradiating cell monolayers (in absence of macroscopic global heating), which means that cytotoxic photo-activated intracellular hot spots are induced by Gel@dye@Au internalized in tumor cells.

## 2.7 Photoacoustic spectroscopy

Photoacoustic (PA) imaging is a biomedical imaging modality able to map optical absorption at centimeter depth in tissues and in sub-millimeter resolution. PA imaging is based on the conversion of the optically absorbed energy in ultrasound waves and operates in the near infrared (NIR, typically between 680 nm and 980 nm) with nanosecond pulses. The optical absorption properties of the hybrid µGels and their modulation with pH and temperature make them potential PA contrast agents. Because of the absorption of Cy in the NIR, we focused on µGels loaded with Cy and performed an *in vitro* characterization at 25°C with a calibrated photoacoustic spectrometer[38] (see details of the experiments in "Materials and Methods"). This study aims to provide (i) a characterization of the optical absorption of the hybrid µGels while the UV-Vis spectra reported above are sensitive to the optical attenuation (or extinction) which is the added contribution of absorption and scattering, and (ii) an evaluation of the hybrid µGels as smart photoacoustic contrast agents. The µGels with dyes and Au NPs are complex structures regarding the interactions with light as both the microgels and the plasmonic nanostructures scatter light and both the dyes and gold nanoparticles assembly absorb light. Moreover, gold nanostructures are both absorbing and scattering with potentially different absorption and scattering spectra[39]. While UV-Vis spectrophotometry measures the attenuation coefficient that combines the scattering and the absorption coefficients, photoacoustic spectroscopy PA is insensitive to scattering and enables to probe only the optical absorption properties. The photoacoustic spectra of Gel@Cy@Au$_{(x)}$ with x= 0, 1 and 5 were measured and are presented in Figure 14. The photostability of the solutions was also evaluated by illuminating the samples with 900 successive laser pulses at the wavelength of 780 nm and monitoring the evolution of the PA coefficients with the number of pulses (Figure 15). The laser fluence on the tubes can be estimated to around 3.8 mJ.cm$^{-2}$. The general shape of the PA spectra of Gel@Cy (without Au NPs loading) recorded at pH= 7.5 is very similar to their UV-vis spectra (displayed in Figure 2, see spectral region 650-900 nm) with an absorption peak found around 790 nm. The ratio between the maximum amplitude for the initial dye concentrations $[\text{Dye}]_0$ = 50 µM and $[\text{Dye}]_0$ = 250 µM is around 6, consistent with a higher loading of dyes in the μGels. Both Gel@Cy samples were found unstable under illumination pulses (Fig. 15) with a progressive decrease of the PA amplitude, which can be explained by the photodegradation of the dye under laser excitation. After 1 incubation (x=1), with Au NPs, the PA spectra of Gel@Cy@Au$_{(1)}$ were significantly modified. Indeed, for [Dye]$_0$ = 50 μM, the PA spectrum of Gel@dye@Au$_{(1)}$ (Fig. 14a) exhibits a peak in the range 750-850 nm that could be attributed to the cyanine, but it appears broader, with a lower amplitude and shifted from *ca.* 790 nm to around 810 nm, compared to Gel@Cy. This peak was not observed when the dye was changed from Cy to MB (see PA spectra of Gel@MB@Au$_{(1)}$ in Fig. S6). It may therefore result from interactions between Cy and Au NPs within the μGels. It is noteworthy that this peak is revealed in the PA spectrum while it is hidden in the UV-vis attenuation spectrum (Fig. 4).

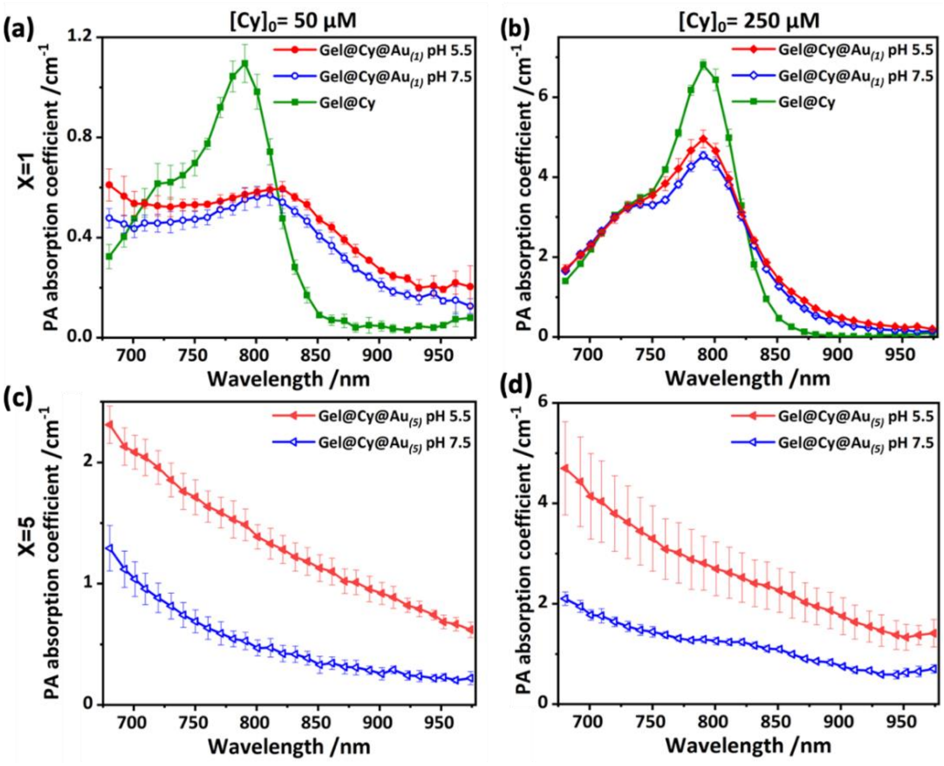

**Figure 14.** Photoacoustic spectra of Gel@Cy (green curves) and Gel@Cy@Au$_{(x=1,5)}$ at pH 7.5 (blue curves) and pH 5.5 (red curves) prepared from two different [Cy]$_0$ concentrations (50 μM and 250 μM). (a) PA spectra of Gel@Cy and Gel@Cy@Au$_{(1)}$ at 0.07 nM prepared from [Cy]$_0$ = 50 μM. (b) PA spectra of Gel@Cy and Gel@Cy@Au$_{(1)}$ at 0.07 nM prepared from [Cy]$_0$ = 250 μM. (c) PA spectra of Gel@Cy@Au$_{(5)}$ at 0.035 nM prepared from [Cy]$_0$ = 50 μM. (d) PA spectra of Gel@Cy@Au$_{(5)}$ at 0.035 nM prepared from [Cy]$_0$ = 250 μM. The amplitude of the PA spectra of all Gel@Cy@Au$_{(5)}$ samples have been multiplied two times for the sake of comparison with their Gel@Cy@Au$_{(1)}$ counterparts, which were concentrated twice for the PA experiments.

Interestingly, an enhanced photostability is observed in Gel@dye@Au$_{(1)}$ prepared from [Dye]$_0$ = 50 µM (Fig. 15). These modifications of the absorption spectra and the enhanced photostability suggest a coupling between the dye and the plasmonic nanoparticles inside the µGels. In contrast, for [Dye]$_0$ = 250 µM, the absorption peak is still at 790 nm (Fig. 15b) and the sample is not photostable, similarly to Gel@Cy, suggesting only a partial coupling between the dyes and Au NPs. This highlights the dominant contribution of the dye over the Au NPs in the absorption spectra of Gel@dye@Au$_{(1)}$ prepared with high dye concentration.

With a further encapsulation of Au NPs (x = 5), the absorption associated with the dye vanishes for [Dye]$_0$ = 50 µM while it is very weak and hardly detectable for [Dye]$_0$ = 250 µM, in agreement with the UV-Vis spectra. However, the PA coefficient at 790 nm is about 2.4 times larger for [Dye]$_0$ = 250 µM than for [Dye]$_0$ = 50 µM, which shows indirectly that the increase in dye loading has an effect on the PA signal. Interestingly, the Gel@dye@Au$_{(5)}$ were found photostable and even an enhancement of the PA signal was observed that could be attributed to a local heating of the surrounding of the plasmonic NPs with the repetitive illuminations, that could enhance the Grüneisen coefficient compared to the initial conditions.

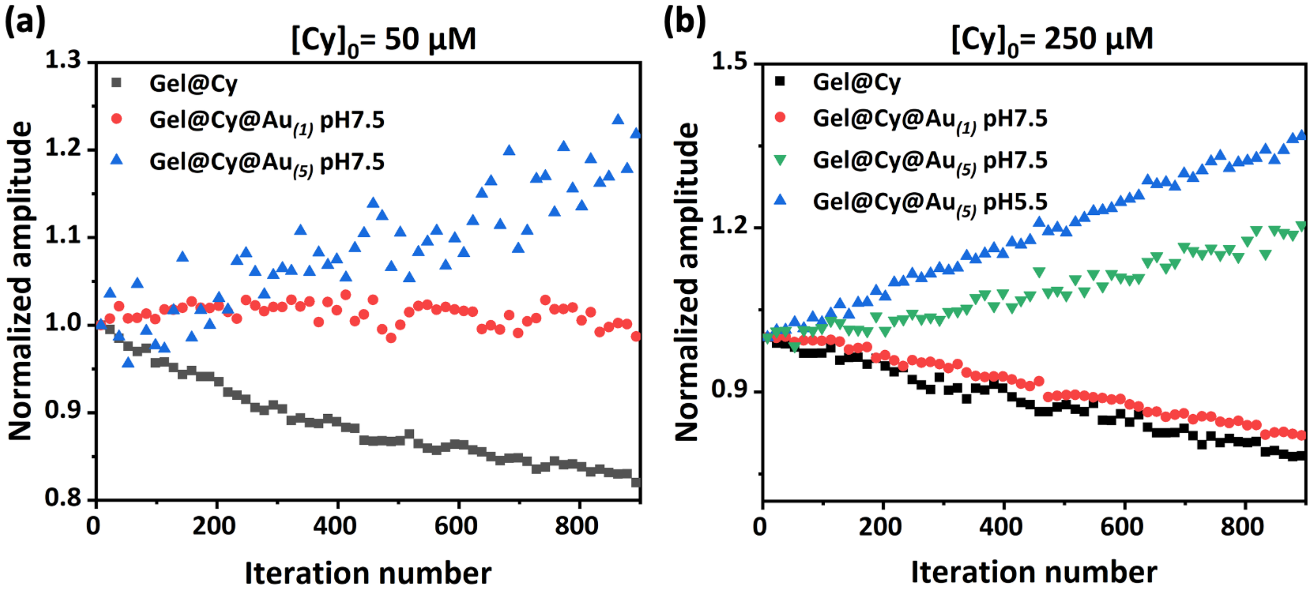

**Figure 15.** Photostability of Gel@Cy and Gel@Cy@Au$_{(1,5)}$ samples prepared from (a) [Cy]$_0$= 50 µM and (b) [Cy]$_0$=250 µM. Each sample was illuminated 900 times at 780nm at 3.8 mJ.cm$^{-2}$. The PA coefficients were averaged over 15 successive laser pulses and were normalized to the first value.

For Gel@dye@Au$_{(1)}$, the PA spectra were only slightly affected by the pH change, in agreement with the UV-vis spectra shown in Figure 7. However, the spectral shape was modified for Gel@dye@Au$_{(5)}$ and a significant increase of the PA coefficient was observed when the pH decreased from pH 7.5 to 5.5. At 800 nm excitation, the PA coefficient increased by a factor of *ca.* 3 and 2 for $[Cy]_0$ = 50 μM and $[Cy]_0$ = 250 μM, respectively (Fig. 15). These results, which indicate a plasmon modification induced by the pH change in agreement with Figure 7 (UV-vis spectra), allow to quantify the influence of pH independently of the scattering modifications induced by the gel contraction. Interestingly, the photostability curve of Gel@dye@Au$_{(5)}$ at pH 5.5 (Fig. 15b) revealed a strong enhancement of the PA signal with the repetitive illuminations, higher than that observed at pH 7.5, suggesting that the pH-induced contraction of the µGels and the resulting plasmon coupling boosts the local increase in temperature. The change in the spectral shape induced by the pH decrease may not be sufficient to discriminate the gels in acidic environment. However, the large increase in the PA signal could be used as a signature to detect that the environment of the contrast agents has become acidic. As slightly acidic microenvironments are observed in cancer tissues or inflamed area due to altered metabolic state[40], the pH sensitivity of the hybrid µGels is an interesting feature for their use as stimuli-responsive photoacoustic contrast agents.

From the PA spectra, the molar absorption coefficients ($\varepsilon_{PA}$) at λ = 800 nm were estimated, by dividing the PA absorption coefficients by the molar concentration of the hybrid µGels. As shown in Table 4, the $\varepsilon_{PA}$ values of the hybrid μGels range between 0.8 and 6.6 × $10^{10}$ $M^{-1}.cm^{-1}$. These values are comparable to the extinction coefficients reported in the literature[41] for anisotropic gold nanostructures such as gold nanocubes ($\varepsilon = 2.19 \times 10^{10}$ $M^{-1}.cm^{-1}$ measured at λ = 808 nm), gold nanocages ($\varepsilon = 1 \times 10^{10}$ $M^{-1}.cm^{-1}$, λ = 802 nm) or poly(sodium 4-styrenesulfonate)-coated gold nanorods ($\varepsilon = 1.45 \times 10^{10}$ $M^{-1}.cm^{-1}$, λ = 785 nm). However, they are far superior to that of isotropic gold nanospheres ($\varepsilon = 3.6 \times 10^{6}$ $M^{-1}.cm^{-1}$ at λ = 506 nm), which are similar to the NPs which were encapsulated in the µGels. Therefore, although the spectral shapes of Gel@Cy@Au$_{(1,5)}$ samples do not exhibit a pronounced peak in the NIR, their high molar absorption coefficients at λ = 800 nm and their pH-sensitivity are key assets for photoacoustic imaging[42].

**Table 4.** Molar absorption coefficients ($\varepsilon_{PA}$) of Gel@Cy and Gel@Cy@Au$_{(x = 1,5)}$ samples at λ = 800 nm, calculated by dividing the PA absorption coefficients by the molar concentration of the hybrid µGels ($7 \times 10^{-11}$ mol.L$^{-1}$) used for the PA experiments.

| ***Samples*** | *$\varepsilon_{PA}$ ($M^{-1}.cm^{-1}$) at pH 7.5* | *$\varepsilon_{PA}$ ($M^{-1}.cm^{-1}$) at pH 5.5* |
|---|---|---|
| | ***[Cy]$_0$ = 50 µM*** | |
| Gel@Cy | $1.4 \times 10^{10}$ | - |
| Gel@Cy@Au$_{(1)}$ | $0.8 \times 10^{10}$ | $0.8 \times 10^{10}$ |
| Gel@Cy@Au$_{(5)}$ | $0.7 \times 10^{10}$ | $2.0 \times 10^{10}$ |
| | ***[Cy]$_0$ = 250 µM*** | |
| Gel@Cy | $9.1 \times 10^{10}$ | - |
| Gel@Cy@Au$_{(1)}$ | $6.1 \times 10^{10}$ | $6.6 \times 10^{10}$ |
| Gel@Cy@Au$_{(5)}$ | $1.8 \times 10^{10}$ | $3.8 \times 10^{10}$ |

## 3. CONCLUSIONS

In summary, we have proposed a straightforward strategy for the rational design of well-defined smart µGels filled with dyes and assemblies of Au NPs. Depending on the initial concentrations of the different building blocks during the assembly process and the number of incubation steps between the µGels and Au NPs, the resulting hybrid materials exhibit various loading levels and well defined internal organization of Au NPs inducing tunable plasmon coupling and unique optical properties. The assembly process was modeled by computer simulations, revealing that nanoparticles can enter like-charged nanogels (despite the repulsive electrostatic forces between them) due to diffusion if the concentration of nanoparticles in the medium is high enough. However, absorption can be enhanced by the presence of: i) short-ranged attractive forces between the monomeric units of the nanogel, the dyes and the nanoparticles; ii) an oppositely charged species (the dye) electrostatically mediating between nanogels and nanoparticles. Characterization of the samples using UV-vis extinction, fluorescence and photoacoustic spectroscopy, TEM, SAXS and DLS revealed that the final hybrid networks integrate the key features of each component, including the high loading capacity and stimuli-responsive behavior of the hydrogel matrix, the fluorescence of the dyes and the optical and photothermal response of plasmon-coupled Au NPs assemblies. Upon temperature or pH stimuli, the hybrid μGels platforms were shown to shrink or swell, resulting in modifications of the organization and interactions of Au NPs trapped within the polymer matrix. In the case of μGels densely filled with Au NPs, such as Gel@dye@Au$_{(5)}$, the temperature or pH stimulation could be used to induce plasmon coupling between the aggregated Au NPs, which resulted in plasmon band broadening and red shift towards the near infrared region (NIR), a key feature for biomedical applications. Photothermal experiments showed that the Gel@dye@Au$_{(5)}$ samples display high heating capacities under NIR laser excitation, with an enhanced effect upon pH decrease, probably due to plasmon coupling. Interestingly, the dyes loaded within the μGels could act as fluorescence tracers to visualize the μGel uptake by colon tumor cells, while the dark cytotoxicity of the three different dyes was much lower in μGels in comparison to the free dyes. Importantly, the photoactivation of tumor cell monolayers exposed to the μGels induced important cell death, that can be used for precision photothermal therapy. Moreover, as determined by photoacoustic spectroscopy, the hybrid μGels exhibit high molar absorption coefficients at $\lambda$ = 800 nm, comparable to the ones of anisotropic gold nanostructures reported in the literature. Another important characteristic is the higher PA amplitude obtained at pH 5.5 compared to pH 7.5 and the enhanced photostability of the hybrid samples compared to free Cy or Gel@Cy. Therefore, although the synthesis methodology proposed herein relies on small, spherical Au NPs, with no particular signal in the NIR, the strategy which consists to assemble them within smart thermo- and pH-sensitive microgel platforms loaded with dyes offers unprecedented opportunities for better controlled photothermal therapy and bioimaging.

# 4. MATERIALS AND METHODS

## 4.1. Materials

Poly(ethylene glycol) diacrylate (OEGDA, $M_n = 575$ g.mol$^{-1}$), Di(ethylene glycol) methyl ether methacrylate 95% ($MEO_2MA$, $M_n = 188.22$ g.mol$^{-1}$ ), Poly(ethylene glycol) methyl ether methacrylate (OEGMA, $M_n = 300$ g.mol$^{-1}$), methacrylic acid (MAA, $M_n = 86.09$ g.mol$^{-1}$) and potassium persulfate (KPS) were purchased from Sigma-Aldrich for the synthesis of microgels. Gold(III) chloride trihydrate ($HAuCl_3 \cdot 3H_2O$), sodium tetrahydridoborate ($NaBH_4$) and tri-sodium citrate dihydrate (NaCi) were purchased from Sigma-Aldrich for the synthesis of gold nanospheres (Au NPs). Hydrochloric acid (37%, AnalaR NORMAPUR) and Sodium Hydroxide (NaOH) were purchased from VWR Chemicals and Sigma-Aldrich, respectively for adjusting the pH. Methylene blue (MB) and rhodamine 6G (R6G) were purchased from Sigma-Aldrich, Cyanine7.5 amine (Cy) was purchased from Lumiprobe. DMEM Medium (Glutamine-Max), Fetal Bovine Serum (FBS), 0.25% Trypsin-EDTA (1X), Dulbecco's Phosphate Buffered Saline [-] $CaCl_2$, [-] $MgCl_2$ (DPBS), Penicillin Streptomycin 100 x (respectively 10,000 Units.mL$^{-1}$ and 10,000 µg.mL$^{-1}$ Streptomycin (PS) and Alamar blue were purchased from Thermofisher Scientific for in *vitro* studies.

## 4.2. Synthesis of gold nanoparticles (Au NPs)

Gold nanospheres were synthesized using $NaBH_4$ as a reducing agent, yielding Au NPs with an average diameter of $3.8 \pm 0.9$ nm. Briefly, 3 mL of 0.1 M aqueous stock solution of sodium citrate, 0.3 mL of 0.1 M gold(III) chloride trihydrate solution and 55.5 mL of ultrapure water were added in a 100 mL flask equipped with a stir bar. The reaction solution was cooled down to 0 °C in ice bath under stirring (600 rpm). Next, 360 µL of 0.1 M $NaBH_4$ solution was added drop by drop until the resulting solution turned red.

### 4.3. Synthesis of oligo(ethylene glycol) methyl ether methacrylate-based microgels

The thermo- and pH-responsive µGels were synthesized as described previously.[13] Briefly, 0.221 mmol MAA, 0.36 mmol OEGMA, 3.3 mmol $MEO_2MA$ and 0.14 mmol OEGDA cross-linker were dissolved in a round-bottom flask with 40 mL of ultrapure water and purged with Ar for 1 h. The reaction solution was then stirred at 400 rpm and heated to 70℃. Then, 5 mg of KPS dissolved in 10 mL purged water were injected and the reaction solution was left to react under Ar atmosphere for 5 h. The reaction was stopped by exposing the flask under air and cooling in ice-water bath for 30 min. The suspension was collected and stored at 4°C.

### 4.4 Assembly process to yield hybrid microgels with fluorescent dyes and Au NPs

1 mL of µGels solution (17.3 $g.L^{-1}$) was washed by 2 cycles of centrifugation at 7000 rpm for 15 min and redispersion in 1 mL of ultrapure (DI) water. The pH of the µGels dispersion was adjusted to 6.8-7.2 by adding NaOH. Various amounts of fluorescent dyes (MB, R6G and Cy)) were added in the µGels solution to prepare the stock Gel@dyes solution (final concentrations of each dye: 50 µM or 250 µM). After 48 hours, the dye-loaded µGels were purified by one cycle of centrifugation and redispersion in 1 mL of ultrapure water. Next, 900 µL of the Au NPs solution ($[Au_{atom}]$= 0.5 $mmol.L^{-1}$, [Au NPs] = 0.27 $µmol.L^{-1}$) were added into 100 µL of dye-loaded µGels solutions. The solution was left to react for 24 hours. The µGels loaded with both Au NPs and dyes were then washed by 1 cycle of centrifugation at 7000 rpm for 15 min/redispersion in water to yield $Gel@dye@Au_{(1)}$ sample. The self-assembly process between the dye-loaded µGels and the Au NPs was repeated up to three and five times, leading to $Gel@dye@Au_{(3)}$ and $Gel@dye@Au_{(5)}$ samples, respectively. The $Gel@Au_{(1, 3, 5)}$ samples were prepared through the same protocol without the addition of dye.

### 4.5. Characterization techniques

The morphology of Gel@dye@Au samples was observed by Tecnai12 transmission electron microscope (FEI, The Netherlands). The hydrodynamic diameter was measured by dynamic light scattering (DLS, Malvern), as a function of pH and temperature. The UV-vis absorption and fluorescence emission spectra were acquired using a cuvette with an optical path length of 1 cm on a UV-Vis spectrometer (Shimadzu 2700, Japan) and a fluorimeter (Hitachi F7000, Japan), respectively. Small angle X-ray scattering (SAXS) experiments were performed at room temperature on SWING beamline (SOLEIL synchrotron, Saint-Aubin, France) with a photon energy of 12 keV and a sample-to-detector (Eiger 4M) distance of 6 m leading to the following q-ranges: $0.001 \leq q$ (Å$^{-1}$) $\leq 0.19$. We recall that the norm of the scattering wave vector is $q = (4\pi/\lambda)\sin(\theta/2)$, where θ is the scattering angle and λ = 1.033 Å is the wave-length. All the intensities are expressed in differential cross-section per volume unit:

$$I(q) \ = \frac{dN(q)}{N_{Tot.}} \frac{1}{\Delta\Omega.\,\delta d} \qquad \text{(eq. 5)}$$

where $\delta d$ is the sample' thickness, $dN(q)/N_{Tot.}$ is the probability for a transmitted photon to be scattered with a momentum transfer $q$ and collected at the solid angle $\Delta\Omega$. $dN(q)$ was measured after azimuthal integration of signal collected on the detector, and $N_{Tot.}$ was estimated from the beam transmitted to a photodiode mounted after the sample. The detector and photodiode were calibrated using water as a reference. The absolute water scattering intensity could be calculated as follows: $I = \rho^2 kT\chi \approx 1.63 \times 10^{-2} cm^{-1}$ at 293 K, with the scattering length density $\rho \approx 9.388 \times 10^{10} cm^{-2}$ , the Boltzmann constant $k$, the temperature $T$ in $K$ and the isothermal compressibility $\chi \approx 10^{-10}\ Pa^{-1}$. Samples were inserted into cylindrical quartz capillaries of 1.5 mm diameter that were sealed and left vertical in the field of gravity. 10 successive frames of 0.5 s each were recorded and compared to check the absence of beam damage. The scattering patterns were always isotropic. Each frame was first radially averaged over all frames and the pure water spectrum was subtracted.

### 4.6. Cell culture, dark cytotoxicity and phototoxicity

CT26 colon cancer cells were cultured in DMEM Medium (Glutamine-Max), FBS 10%, Penicillin Streptomycin 1x at 37°C and 5% $CO_2$. Dark cytotoxicity of µGels was assessed on CT26 colon cancer cells. Cells were seeded at a density of 10,000 cells/well in 500 µL of medium in 48 well plate and incubated overnight. Then, the medium was renewed with 350 µL of fresh medium containing 5 µM Gel@dye@Au$_{(x)}$ prepared from [Dye]$_0$ = 50 µM or 250 µM and with different Au NPs loading (x = 1 and x = 5). After 24 h of incubation, the medium was removed and the excess of NPs was washed with 500 µL of PBS once. Then, 200 µL of DMEM without phenol red were added to each well. Cells were incubated for additional 18h and cytotoxicity was investigated by replacing the medium with fresh 200 µL medium without FBS containing 10% alamar Blue. 200 µL of each 48 wells were transferred to wells from a non-transparent 96 well plate and fluorescence intensity was measured in a plate reader (Ex. 560 nm, Em. 590 nm) (SpectraMax iD3, Molecular Devices, US). Phototoxicity was measured in the same way as dark toxicity but a photothermal treatment was performed before the 18 h incubation. For this, each well was exposed for 10 minutes to an 808 nm laser at 1 or 2 W/cm$^2$ (CNI FC series Fiber Coupling Laser system).

### 4.7. Cell uptake of hybrid µGels

CT26-Luc cells were seeded in 6-well plates at a density of $1.2\times10^6$ cells/well and cultured for 24 h. Then, the culture medium was replaced by 2 mL of medium containing the desired concentration of Gel@dye@Au$_{(x)}$ (prepared from [Dye]$_0$ = 50 µM and 250 µM, with x = 1 and x = 5) and incubated with cells for 5 min at 4°C, 6 h and 24 h at 37°C. After incubation, cells were washed by PBS for three times and the nuclei were stained by hoechst 33342. Cellular imaging was performed with a Cell Insight$^{TM}$ CX7 HCS Platform (Thermofisher) (Hoechst: Ex. 405 nm, Em. 446/37 nm; R6G: Ex. 561 nm, Em. 600/41 nm; MB: Ex. 647 nm, Em. 677/34 nm; Cy: Ex. 785 nm, Em. 805 nm).

## 4.8. Photothermal experiments

Gel@dye@Au solutions with fixed μGel (1.73 mg.mL$^{-1}$) and dye concentration (with initial dye concentration $[Dye]_0$ = 50 μM) but with different Au NPs loading (from no Au NPs to 50 mg.g$^{-1}$ for x = 1 and 250 mg.g$^{-1}$ for x = 5) were exposed to a continuous wave CNI FC series Fiber Coupling Laser system with a wavelength of 808 nm and a density of 1.1 W.cm$^{-2}$ for 300 s. The density was calculated by dividing the power after fiber, which is measured using a power meter PM400K5 thorlabs, with the surface of the laser beam. The temperature of samples was measured in Eppendorf micro centrifuge tubes of 0.5 mL. Illumination from the laser was directed directly on the sample from the top, thanks to a fiber. The infrared camera FLIR t430sc recorded the temperature from the side. From the film thus obtained, we are able to delineate a Region of Interest (ROI) around the hot spot. The temperature obtained is the average temperature of each pixel located in this ROI. The specific absorption rate (SAR) was measured as follows. The initial temperature slope, dT/dt, after laser switch-on, was measured, and SAR was calculated according to: SAR = CV/m × dT/dt, where m is the total mass of the materials in the sample (here m = mass of Au NPs for x=1 or x=5, calculated from Table 1: $m_{Au}$=8.65 µg for x=1 and $m_{Au}$=43.25 µg for x=5), C is the specific heat capacity of the sample ($C_{water}$ = 4185 J.L$^{-1}$.K$^{-1}$), and V is the sample volume (V=100 µL).

## 4.9. Photoacoustic spectroscopy

A calibrated photoacoustic (PA) spectrometer based on a conventional photoacoustic system was used. The system is detailed in Reference[38]. Only the main specifications are presented here. The sample solutions were injected in PTFE tubes of inner diameter 200 µm, immersed in a water bath maintained at 25°C, and imaged successively at 30 optical wavelengths between 680 nm and 970 nm by steps of 10 nm. A tunable nanosecond laser with a pulse repetition frequency of 20 Hz was used. The laser fluence at 780 nm was around 3.8 mJ.cm$^{-2}$. 15 successive scans of the optical wavelengths were performed and the ultrasound data were averaged before the image formation. Blank datasets were acquired by filling the tubes with ultrapure water and were subtracted to the ultrasound signals for a baseline correction. Photoacoustic images were formed and the amplitude of the tube on the image was measured for each optical wavelength. A calibration was performed with a reference solution of pentahydrate copper (II) sulfate at 250 mM to convert this amplitude in a PA coefficient directly proportional to the decadic absorption coefficient of the solution. The proportionality factor between the PA coefficient and the decadic absorption coefficient is named photoacoustic generation efficiency (PGE) and is the product of the photothermal conversion efficiency (conversion efficiency of the absorbed optical energy to heat) and the Grüneisen coefficient relative to water (conversion of the heat energy to ultrasound waves). The PGE is equal to one for a sample for which the absorbed energy is fully converted into pressure in a medium with the Grüneisen coefficient of the water. The PA coefficient is expressed in $cm^{-1}$, and is equal to the decadic absorption coefficient for a solution with a PGE equal to 1. The PGE of the microgels was not determined here. For each sample, the PA coefficient was measured eight times (two injections in four tubes). The PA spectra correspond to the median value and the error bars to the median absolute deviation with a scale factor 1.4826. 0.1 M HCl was used to adjust the pH of the hybrids for the Gel@Cy@Au samples studied at pH = 5.5. The decrease in pH from 7.5 to 5.5 was performed 30 min before the spectral measurements. To keep the measurement range within the detection limit of PA setup, we concentrated the hybrid gels with low Au NPs loading (Gel@Cy@$Au_{(1)}$ with x = 1) twice for PA measuring. It is worth noting that due to the fact that the hybrid gels easily adhere to the wall of the centrifuge tubes during the preparation and transfer process, a certain degree of sample loss was observed. The photostability of the solutions was evaluated by illuminating the sample with 900 successive laser pulses at 780 nm with a laser fluence of 3.8 $mJ.cm^{-2}$. The PA coefficient was assessed for each laser pulse and the mean of 15 successive iterations was computed for a better signal to noise ratio.

## ☐ ASSOCIATED CONTENT

**Supporting Information:** Additional experimental details, materials, and methods, including TEM and fluorescence microscopy images, DLS data, SAXS, PA spectra and coarse-grained simulation results.

## ☐ AUTHOR INFORMATION

### Corresponding Author

* Claire Mangeney. E-mail : claire.mangeney@u-paris.fr
* Florence Gazeau. Email: florence.gazeau@univ-paris-diderot.fr
* Yun Luo. Email : yun.luo@u-paris.fr

### Author Contributions

All authors have given approval to the final version of the manuscript.

### Notes

Any additional relevant notes should be placed here.

## ☐ ACKNOWLEDGMENT

A. M.-M., M. Q.-P and M. M. R.-T are grateful for funding from “Consejería de Economía, Conocimiento, Empresas y Universidad, Junta de Andalucía, Programa Operativo FEDER Andalucía 2014-2020”, Project P20_00138, “Consejería de Conocimiento, Investigación y Universidad, Junta de Andalucía” and European Regional Development Fund (ERDF), Project SOMM17/6105/UGR. The financial support by Ministerio de Ciencia e Innovación, Projects PGC2018-098770-B-I00 and PID2020-116615RA-I00, is also thanked. This work is supported by the scholarship from China Scholarship Council (CSC) under the Grant CSC N° 201806240315. This study was supported by the IdEx Université Paris Cité, ANR-18-IDEX-0001 (plateforme IVETh and Emergence FLORIM) and by the Region Ile de France under the convention SESAME 2019 - IVETh (n° EX047011). We thank Dmitry Ayollo for help in Cell Insight experiments and Dr Thomas Bizien (Soleil synchrotron, Swing beamline) for his assistance with carrying out SAXS experiments. Soleil synchrotron is gratefully acknowledged for beam time allocation.

## ☐ REFERENCES

1. Zhao, N.; Yan, L.; Zhao, X.; Chen, X.; Li, A.; Zheng, D.; Zhou, X.; Dai, X.; Xu, F.-J., Versatile types of organic/inorganic nanohybrids: from strategic design to biomedical applications. *Chemical reviews* **2018,** *119* (3), 1666-1762.
2. Park, W.; Shin, H.; Choi, B.; Rhim, W.-K.; Na, K.; Han, D. K., Advanced hybrid nanomaterials for biomedical applications. *Progress in Materials Science* **2020,** *114*, 100686.
3. Wang, C.; Cui, Q.; Wang, X.; Li, L., Preparation of hybrid gold/polymer nanocomposites and their application in a controlled antibacterial assay. *ACS Applied Materials & Interfaces* **2016,** *8* (42), 29101-29109.
4. Hood, M. A.; Mari, M.; Muñoz-Espí, R., Synthetic strategies in the preparation of polymer/inorganic hybrid nanoparticles. *Materials* **2014,** *7* (5), 4057-4087.
5. Seyfoori, A.; Seyyed Ebrahimi, S.; Samiei, E.; Akbari, M., Multifunctional hybrid magnetic microgel synthesis for immune-based isolation and post-isolation culture of tumor cells. *ACS Applied Materials & Interfaces* **2019,** *11* (28), 24945-24958.
6. Bhol, P.; Mohanty, P. S., Smart microgel-metal hybrid particles of PNIPAM-co-PAA@ AgAu: synthesis, characterizations and modulated catalytic activity. *Journal of Physics: Condensed Matter* **2020,** *33* (8), 084002.
7. Boularas, M.; Deniau-Lejeune, E.; Alard, V.; Tranchant, J.-F.; Billon, L.; Save, M., Dual stimuli-responsive oligo (ethylene glycol)-based microgels: insight into the role of internal structure in volume phase transitions and loading of magnetic nanoparticles to design stable thermoresponsive hybrid microgels. *Polymer Chemistry* **2016,** *7* (2), 350-363.

8. Cazares-Cortes, E.; Espinosa, A.; Guigner, J.-M.; Michel, A.; Griffete, N.; Wilhelm, C.; Ménager, C., Doxorubicin intracellular remote release from biocompatible oligo (ethylene glycol) methyl ether methacrylate-based magnetic nanogels triggered by magnetic hyperthermia. *ACS Applied Materials & Interfaces* **2017,** *9* (31), 25775-25788.

9. Cazares-Cortes, E.; Wilhelm, C.; Perez, J. E.; Espinosa, A.; Casale, S.; Michel, A.; Abou-Hassan, A.; Ménager, C., Tuning the load of gold and magnetic nanoparticles in nanogels through their design for enhanced dual magneto-photo-thermia. *Chemical Communications* **2021,** *57* (48), 5945-5948.

10. Lutz, J.-F.; Stiller, S.; Hoth, A.; Kaufner, L.; Pison, U.; Cartier, R., One-pot synthesis of PEGylated ultrasmall iron-oxide nanoparticles and their in vivo evaluation as magnetic resonance imaging contrast agents. *Biomacromolecules* **2006,** *7* (11), 3132-3138.

11. Ulasan, M.; Yavuz, E.; Bagriacik, E. U.; Cengeloglu, Y.; Yavuz, M. S., Biocompatible thermoresponsive PEGMA nanoparticles crosslinked with cleavable disulfide-based crosslinker for dual drug release. *Journal of Biomedical Materials Research Part A* **2015,** *103* (1), 243-251.

12. Kuppe, C.; Rusimova, K. R.; Ohnoutek, L.; Slavov, D.; Valev, V. K., “Hot” in Plasmonics: Temperature-Related Concepts and Applications of Metal Nanostructures. *Advanced Optical Materials* **2020,** *8* (1), 1901166.

13. Jeong, H.-H.; Choi, E.; Ellis, E.; Lee, T.-C., Recent advances in gold nanoparticles for biomedical applications: from hybrid structures to multi-functionality. *Journal of Materials Chemistry B* **2019,** *7* (22), 3480-3496.

14. Wu, Q.; Peng, R.; Luo, Y.; Cui, Q.; Zhu, S.; Li, L., Antibacterial activity of porous gold nanocomposites via NIR light-triggered photothermal and photodynamic effects. *ACS Applied Bio Materials* **2021,** *4* (6), 5071-5079.

15. Cheheltani, R.; Ezzibdeh, R. M.; Chhour, P.; Pulaparthi, K.; Kim, J.; Jurcova, M.; Hsu, J. C.; Blundell, C.; Litt, H. I.; Ferrari, V. A., Tunable, biodegradable gold nanoparticles as contrast agents for computed tomography and photoacoustic imaging. *Biomaterials* **2016,** *102*, 87-97.

16. Balfourier, A.; Luciani, N.; Wang, G.; Lelong, G.; Ersen, O.; Khelfa, A.; Alloyeau, D.; Gazeau, F.; Carn, F., Unexpected intracellular biodegradation and recrystallization of gold nanoparticles. *Proceedings of the National Academy of Sciences* **2020,** *117* (1), 103-113.

17. Yu, M.; Xu, J.; Zheng, J., Renal clearable luminescent gold nanoparticles: from the bench to the clinic. *Angewandte Chemie International Edition* **2019,** *58* (13), 4112-4128.

18. Dam, D. H. M.; Culver, K. S.; Kandela, I.; Lee, R. C.; Chandra, K.; Lee, H.; Mantis, C.; Ugolkov, A.; Mazar, A. P.; Odom, T. W., Biodistribution and in vivo toxicity of aptamer-loaded gold nanostars. *Nanomedicine: Nanotechnology, Biology and Medicine* **2015,** *11* (3), 671-679.

19. Ali, M. R.; Rahman, M. A.; Wu, Y.; Han, T.; Peng, X.; Mackey, M. A.; Wang, D.; Shin, H. J.; Chen, Z. G.; Xiao, H., Efficacy, long-term toxicity, and mechanistic studies of gold nanorods photothermal therapy of cancer in xenograft mice. *Proceedings of the National Academy of Sciences* **2017,** *114* (15), E3110-E3118.

20. Kim, S.-E.; Lee, B.-R.; Lee, H.; Jo, S. D.; Kim, H.; Won, Y.-Y.; Lee, J., Near-infrared plasmonic assemblies of gold nanoparticles with multimodal function for targeted cancer theragnosis. *Scientific reports* **2017,** *7* (1), 1-10.

21. Quesada-Pérez, M.; Maroto-Centeno, J.-A.; Ramos-Tejada, M. a. d. M.; Martín-Molina, A., Coarse-Grained simulations of solute diffusion in crosslinked flexible hydrogels. *Macromolecules* **2022,** *55* (5), 1495-1504.

22. Pérez-Mas, L.; Martín-Molina, A.; Quesada-Pérez, M., Coarse-grained Monte Carlo simulations of nanogel–polyelectrolyte complexes: electrostatic effects. *Soft Matter* **2020,** *16* (12), 3022-3028.

23. Zhai, Y.; Ran, W.; Su, J.; Lang, T.; Meng, J.; Wang, G.; Zhang, P.; Li, Y., Traceable bioinspired nanoparticle for the treatment of metastatic breast cancer via NIR-trigged intracellular delivery of methylene blue and cisplatin. *Advanced Materials* **2018,** *30* (34), 1802378.

24. Yoon, H. K.; Ray, A.; Koo Lee, Y.-E.; Kim, G.; Wang, X.; Kopelman, R., Polymer–protein hydrogel nanomatrix for stabilization of indocyanine green towards targeted fluorescence and photoacoustic bio-imaging. *Journal of Materials Chemistry B* **2013,** *1* (41), 5611-5619.

25. Golz, E. K.; Vander Griend, D. A., Modeling methylene blue aggregation in acidic solution to the limits of factor analysis. *Analytical chemistry* **2013,** *85* (2), 1240-1246.
26. Flory, P. J.; Rehner Jr, J., Statistical mechanics of cross-linked polymer networks I. Rubberlike elasticity. *The journal of chemical physics* **1943,** *11* (11), 512-520.
27. Flory, P. J.; Rehner, J., Statistical mechanics of cross-Linked polymer networks II. Swelling. *The journal of chemical physics* **1943,** *11* (11), 521-526.
28. Quesada-Pérez, M.; Maroto-Centeno, J. A.; Forcada, J.; Hidalgo-Alvarez, R., Gel swelling theories: the classical formalism and recent approaches. *Soft Matter* **2011,** *7* (22), 10536-10547.
29. Cooper, D.; Uhm, H.; Tauzin, L. J.; Poddar, N.; Landes, C. F., Photobleaching lifetimes of cyanine fluorophores used for single-molecule Förster resonance energy transfer in the presence of various photoprotection systems. *ChemBioChem* **2013,** *14* (9), 1075-1080.
30. Bera, A.; Bagchi, D.; Pal, S. K., Improvement of Photostability and NIR Activity of Cyanine Dye through Nanohybrid Formation: Key Information from Ultrafast Dynamical Studies. *The Journal of Physical Chemistry A* **2019,** *123* (35), 7550-7557.
31. Kutushov, M.; Gorelik, O., Low concentrations of Rhodamine-6G selectively destroy tumor cells and improve survival of melanoma transplanted mice. *Neoplasma* **2013,** *60* (3), 262-273.
32. Pakavathkumar, P.; Sharma, G.; Kaushal, V.; Foveau, B.; LeBlanc, A. C., Methylene blue inhibits caspases by oxidation of the catalytic cysteine. *Scientific reports* **2015,** *5* (1), 1-13.
33. Salahuddin, N.; Akelah, A.; Elnagar, M.; Abdelwahab, M. A., Antibacterial and cytotoxicity of methylene blue loaded-cellulose nanocarrier on breast cancer cell line. *Carbohydrate Polymer Technologies and Applications* **2021,** *2*, 100138.
34. Li, Q.; Liu, C.-G.; Yu, Y., Separation of monodisperse alginate nanoparticles and effect of particle size on transport of vitamin E. *Carbohydrate polymers* **2015,** *124*, 274-279.
35. Switacz, V. K.; Wypysek, S. K.; Degen, R.; Crassous, J. J.; Spehr, M.; Richtering, W., Influence of size and cross-linking density of microgels on cellular uptake and uptake kinetics. *Biomacromolecules* **2020,** *21* (11), 4532-4544.
36. Banerjee, A.; Billey, L. O.; Shelver, W. L., Uptake and toxicity of polystyrene micro/nanoplastics in gastric cells: Effects of particle size and surface functionalization. *PloS one* **2021,** *16* (12), e0260803.
37. Sanchala, D.; Bhatt, L. K.; Pethe, P.; Shelat, R.; Kulkarni, Y. A., Anticancer activity of methylene blue via inhibition of heat shock protein 70. *Biomedicine & Pharmacotherapy* **2018,** *107*, 1037-1045.
38. Lucas, T.; Sarkar, M.; Atlas, Y.; Linger, C.; Renault, G.; Gazeau, F.; Gateau, J., Calibrated photoacoustic spectrometer based on a conventional imaging system for in vitro characterization of contrast agents. *Sensors* **2022,** *22* (17), 6543.
39. Jain, P. K.; Lee, K. S.; El-Sayed, I. H.; El-Sayed, M. A., Calculated absorption and scattering properties of gold nanoparticles of different size, shape, and composition: applications in biological imaging and biomedicine. *The journal of physical chemistry B* **2006,** *110* (14), 7238-7248.
40. Chen, Q.; Liu, X.; Chen, J.; Zeng, J.; Cheng, Z.; Liu, Z., A self-assembled albumin-based nanoprobe for in vivo ratiometric photoacoustic pH imaging. *Advanced Materials* **2015,** *27* (43), 6820-6827.
41. Weber, J.; Beard, P. C.; Bohndiek, S. E., Contrast agents for molecular photoacoustic imaging. *Nature methods* **2016,** *13* (8), 639-650.
42. Nguyen, V. P.; Qian, W.; Li, Y.; Liu, B.; Aaberg, M.; Henry, J.; Zhang, W.; Wang, X.; Paulus, Y. M., Chain-like gold nanoparticle clusters for multimodal photoacoustic microscopy and optical coherence tomography enhanced molecular imaging. *Nature Communications* **2021,** *12* (1), 34.

# Table of Contents